



## Updated Combination of Searches for the Standard Model Higgs Boson at the DØ Experiment in $9.7 \text{ fb}^{-1}$ of Data

The DØ Collaboration  
URL <http://www-d0.fnal.gov>

(Dated: April 28, 2018)

Searches for standard model Higgs boson production at the DØ experiment in  $p\bar{p}$  collisions at  $\sqrt{s} = 1.96 \text{ TeV}$  are carried out for Higgs boson masses ( $m_H$ ) in the range  $100 \leq m_H \leq 200 \text{ GeV}$ . Most of these searches use the full Run II data set, corresponding to an integrated luminosity of  $9.7 \text{ fb}^{-1}$ , and are combined to maximize the sensitivity to the standard model Higgs boson. In absence of a significant excess above the background expectation, 95% confidence level upper limits are set on the production cross section for a standard model Higgs boson. The upper limits are found to be a factor of 2.11 (0.73) times the predicted standard model cross section for  $m_H = 115$  (165) GeV. Under the background-only hypothesis, the corresponding expected limit is 1.46 (0.72) times the standard model prediction. At the same confidence level, these analyses exclude a standard model Higgs boson with a mass in the range  $159 < m_H < 170 \text{ GeV}$ , while the *a priori* expected exclusion is  $156 < m_H < 173 \text{ GeV}$ . In the range  $120 < m_H < 140 \text{ GeV}$ , the data exhibit an excess over the background prediction of approximately two Gaussian standard deviations.

*Preliminary Results for Summer 2012 Conferences*

## I. INTRODUCTION

Despite its success as a predictive tool, the standard model (SM) of particle physics remains incomplete without a means to explain electroweak symmetry breaking. The simplest proposed mechanism involves the introduction of a complex doublet of scalar fields that generate the masses of elementary particles via their mutual interactions. After accounting for longitudinal polarizations for the electroweak bosons, this so-called Higgs mechanism also gives rise to a single scalar boson with an unpredicted mass. Direct searches in  $e^+e^- \rightarrow Z^* \rightarrow ZH$  at the Large Electron Positron (LEP) collider yielded a lower mass limit of  $m_H > 114.4$  GeV [1], at 95% confidence level (C.L.). Precision electroweak data, including the latest  $W$  boson mass measurements from CDF [2] and D0 [3], constrain the mass of a SM Higgs boson to  $m_H < 152$  GeV [4] at 95% C.L. Direct searches at the CMS [5] and ATLAS [6] experiments limit the SM Higgs boson to have a mass between 115.5 GeV and 127 GeV at 95% C.L. Additionally, both LHC experiments report a signal-like excess around a mass of 125 GeV.

In this note, we combine the results of direct searches for SM Higgs bosons in  $p\bar{p}$  collisions at  $\sqrt{s} = 1.96$  TeV recorded with the  $D\bar{O}$  experiment [7]. The analyses combined here seek signals of Higgs bosons produced through gluon-gluon fusion ( $gg \rightarrow H$ ), in association with vector bosons ( $q\bar{q} \rightarrow VH$ , where  $V = W, Z$ ), and through vector boson fusion (VBF) ( $q\bar{q} \rightarrow q\bar{q}H$ ). The Higgs boson decay modes studied are  $H \rightarrow b\bar{b}$ ,  $H \rightarrow W^+W^-$ ,  $H \rightarrow \tau^+\tau^-$ , and  $H \rightarrow \gamma\gamma$ . Most analyses utilize data corresponding to an integrated luminosity of  $9.7 \text{ fb}^{-1}$ , collected during the data-taking period 2002-2011 (Run II). In order to facilitate proper combination of signals, the analyses were constructed to be mutually exclusive after analysis selections. The searches are organized into analysis sub-channels comprising different production, decay, and final state particle configurations designed to maximize the sensitivity for a particular Higgs boson production and decay mode. These sub-channels, typically having different sensitivity, are analyzed separately and combined at the end in order to maximize the search sensitivity. Details on the individual analyses and the improvements since the last combination [8] are provided in the following section.

## II. SUMMARY OF CONTRIBUTING ANALYSES

A summary of the analyses used in this combination is given in Table I. The most sensitive analyses for Higgs boson masses below approximately 130 GeV are those searching for  $H \rightarrow b\bar{b}$  in association with a leptonically decaying weak vector boson. To help isolate these  $H \rightarrow b\bar{b}$  decays, the analyses use an algorithm to identify jets that are consistent with containing the decay of a  $b$  quark ( $b$ -tagging). Several kinematic variables sensitive to displaced jet vertices and jet tracks with large transverse impact parameters relative to the hard-scatter vertices are combined in a boosted decision tree based  $b$ -tagging discriminant. This algorithm is an upgraded version of the neural network  $b$ -tagger used previously [9]. By adjusting a minimum requirement on the  $b$ -tagging output, a spectrum of increasingly stringent  $b$ -tagging operating points is achieved, with a range of signal efficiencies and purities.

The  $ZH \rightarrow \ell\ell b\bar{b}$  ( $\ell = e, \mu$ ) analysis [10] requires two isolated charged leptons and two or three hadronic jets, at least

TABLE I: List of analysis channels ( $V = W, Z$  and  $\ell = e, \mu$ ) with the corresponding integrated luminosities, final variables used for setting limits, and mass range studied. See Section II for details. All conference notes can be found from Ref. [20].

Channel	Luminosity ( $\text{fb}^{-1}$ )	Final Variable	$m_H$ Range	Reference
$ZH \rightarrow \ell\ell b\bar{b}$ , 4 (lepton) $\times$ 2 ( $b$ -tag) $\times$ 2 ( $t\bar{t}$ ) categories	9.7	Decision Tree Discriminant	100–150	[10]
$ZH \rightarrow \nu\bar{\nu} b\bar{b}$ , 2 ( $b$ -tag) categories	9.5	Decision Tree Discriminant	100–150	[11]
$WH \rightarrow \ell\nu b\bar{b}$ , 4 ( $b$ -tag) $\times$ 2 (jet) categories	9.7	Decision Tree Discriminant	100–150	[12]
$H \rightarrow W^+W^- \rightarrow ee/\mu\mu\nu\nu$ , $2 \times 2 + 1$ (jet $\times$ $WW$ ) categories	9.7	Decision Tree Discriminant	115–200	[13]
$H \rightarrow W^+W^- \rightarrow e^\pm\nu\mu^\mp\nu$ , 3 (jet) categories	9.7	Decision Tree Discriminant	115–200	[13]
$VH \rightarrow e^\pm\mu^\pm + X$	9.7	Decision Tree Discriminant	115–200	[14]
$VH \rightarrow ee\mu/\mu\mu e + X$	9.7	Decision Tree Discriminant	100–200	[15]
$VH \rightarrow \ell\nu q\bar{q}q\bar{q}$ , 2 (low $b$ -tag) categories	9.7	Decision Tree Discriminant	100–200	[12]
$H \rightarrow \gamma\gamma$	9.7	Decision Tree Discriminant	100–150	[16]
$H + X \rightarrow \mu^\pm\tau_{had}^\mp + \leq 1j$	7.3	Neural Network Discriminant	115–200	[17]
$VH \rightarrow \tau\tau\mu + X$	7.0	Summed $ p_T $ of all objects	115–200	[18]
$H \rightarrow W^+W^- \rightarrow \ell\nu q\bar{q}$	5.4	Decision Tree Discriminant	155–200	[19]

one of which must pass a tight  $b$ -tag requirement. The events are then divided into “double-tag” and “single-tag” sub-channels depending on whether or not a second jet passes a loose  $b$ -tag requirement. The typical efficiency and fake rate for taggable [9] jets for the loose (tight)  $b$ -tag selection is about 80% (50%) and 10% (1%), respectively. The analysis uses decision tree discriminants to provide the final variables for setting limits. For this iteration of the analysis, a two-step process is applied. First, the events are divided into  $t\bar{t}$ -depleted or  $t\bar{t}$ -enriched sub-channels using decision trees trained to discriminate signal from the  $t\bar{t}$  backgrounds in each lepton and  $b$ -tag sub-channel. This allows to isolate two regions with different signal-to-background. Final discriminants are then constructed to separate signal from all backgrounds. The limit is calculated using the output distributions of the final discriminants for both the  $t\bar{t}$ -depleted and  $t\bar{t}$ -enriched samples. The better signal-to-background discrimination, in addition to other optimizations in the event selection, result in a sensitivity improvement of approximately 10–14% compared to the previous result [21].

The  $ZH \rightarrow \nu\bar{\nu}b\bar{b}$  analysis [11] selects events with large  $\cancel{E}_T$  and two hadronic jets. A sizable fraction of signal comes from  $WH \rightarrow \ell\nu b\bar{b}$  events in which the charged lepton does not pass the criteria for the  $WH \rightarrow \ell\nu b\bar{b}$  analysis. However, events with leptons that pass the criteria for the  $WH \rightarrow \ell\nu b\bar{b}$  analysis are rejected to ensure orthogonality between the two analyses. Track-based missing transverse momentum and  $\cancel{E}_T$  significance variables are used to reduce instrumental backgrounds with false  $\cancel{E}_T$ . The multijet background is further reduced by employing a dedicated decision tree discriminant before  $b$ -tagging. This analysis defines an event-level  $b$ -tag quality by summing the  $b$ -tag outputs from the two jets. Two orthogonal  $b$ -tag sub-channels are then defined. The “tight-tag” sub-channel requires that both jets pass rather tight  $b$ -tag criteria, while the “medium-tag” sub-channel allows for the criteria on one of the jets to be relaxed provided that the other jet has a sufficiently high  $b$ -tag output. Decision trees classifiers trained separately for the different  $b$ -tagging categories are used as the final discriminant. Improved training of these discriminants by using larger Monte Carlo statistics leads to a gain in sensitivity of approximately 10% relative to the previous result [22].

The  $WH \rightarrow \ell\nu b\bar{b}$  analysis [12] exploits topologies with a charged lepton, missing energy, and two or three hadronic jets. Decision trees are used to discriminate against the multijet background. Using the average of the two highest  $b$ -tag outputs from all selected jets, six orthogonal  $b$ -tag categories are defined. The two categories with the lowest  $b$  jet purity are removed to avoid overlap with the  $H \rightarrow W^+W^- \rightarrow \ell\nu q\bar{q}$  analysis [19], while the remaining categories define the four  $b$ -tag sub-channels used in this analysis. A final decision tree discriminant is constructed for each lepton flavor, jet multiplicity, and  $b$ -tag sub-channel. In addition to kinematic variables, the inputs to the final discriminants include the output from the  $b$ -tagger and the output from the multijet discriminant. Changes with respect to the previous result [23] include extending from three to four the number of  $b$ -tag sub-channels considered, improving the multivariate treatment, and increasing the pseudo-rapidity acceptance of muons, ultimately improving the sensitivity by approximately 10–17%.

The  $H \rightarrow W^+W^- \rightarrow \ell^\pm\nu\ell^\mp\nu$  analyses target Higgs boson decays to two  $W$  bosons and consider the three dominant production mechanisms: gluon-gluon fusion, associated production, and vector-boson fusion. The three dominant search channels are  $e^+\nu e^-\nu$ ,  $e^\pm\nu\mu^\mp\nu$ , and  $\mu^+\nu\mu^-\nu$  [13]. Events are characterized by large  $\cancel{E}_T$  and two oppositely-charged isolated leptons, which can have rather low transverse momentum for  $m_H < 2m_W$ , where at least one of the  $W$  bosons is off-mass shell. The presence of neutrinos in the final state prevents the reconstruction of the candidate Higgs boson mass. Each final state is further subdivided according to the number of jets in the event: zero, one, or two or more jets. This allows the individual discriminants to separate differing contributions of signal and background processes more effectively. However, this introduces the need to evaluate the systematic uncertainties carefully in each jet category, as discussed in Section III. The  $e^+\nu e^-\nu$  and  $\mu^+\nu\mu^-\nu$  channels use decision trees discriminants to reduce the dominant Drell-Yan background, while the  $e^\pm\nu\mu^\mp\nu$  channel uses  $\cancel{E}_T$ -related variables to remove backgrounds. Decision trees are used as the final discriminants, including input kinematic as well as topological variables (e.g.  $b$ -tagging information in the case of sub-channels with jets). The events in the  $e^+\nu e^-\nu$  and  $\mu^+\nu\mu^-\nu$  channels in the zero and one jet categories are further subdivided in two samples each using dedicated decision trees that enhance or reduce the contribution from the non-resonant  $WW$  background. All sub-samples are used in the limit setting, with the additional channels significantly constraining the uncertainty on the  $WW$  cross-section. In addition, the integrated luminosity of the sample used in the  $e^+\nu e^-\nu$  channel has been increased from 8.6 to 9.7 fb<sup>-1</sup>, including data which had not been considered in the previous analysis. These changes led to an improvement in sensitivity of approximately 5–10% relative to the previous result [24].

Decays involving tau leptons are included in two ways. A dedicated analysis [17] ( $\mu\tau_{\text{had}}$ ) using 7.3 fb<sup>-1</sup> of data studying the final state involving a muon and a hadronic tau decay plus up to one jet. Final states involving other tau decays and mis-identified hadronic tau decays are included in the  $H \rightarrow W^+W^- \rightarrow \ell^\pm\nu\ell^\mp\nu$  analyses. The  $\mu\tau_{\text{had}}$  channel uses neural networks as the final discriminant. In addition, the trilepton search for  $\tau\tau\mu$ , discussed below, is primarily sensitive to  $H \rightarrow \tau^+\tau^-$ .

For  $VH \rightarrow VWW$  production, we consider final states with three charged leptons [15, 18] ( $ee\mu$ ,  $\mu\mu e$ , and  $\tau\tau\mu$ ), as well as the dilepton final state containing an electron and muon with the same charge [14] ( $e^\pm\mu^\pm + X$ ), which benefits greatly from the suppression of Drell-Yan background. The  $ee\mu$  and  $\mu\mu e$  analyses use decision trees as final discriminants, while the  $\tau\tau\mu$  analysis uses the scalar sum of the  $p_T$  from all objects. The  $\mu\mu e$  search has improved the signal-to-background discrimination by splitting the sample in three orthogonal sub-channels (without  $Z$  boson candidate, or with  $Z$  boson candidate and high/low missing transverse energy significance) and including jet-related information in the multivariate analysis. This leads to an improvement in sensitivity of approximately 10–20% relative to the previous result [25]. The  $e^\pm\mu^\pm + X$  analysis uses a two step multivariate approach. First, a decision tree is used to remove most of the dominant backgrounds from multijet and  $W$ +jets/ $\gamma$  events. Then a final decision tree is used to discriminate signal from the remaining background.

We also include analyses that search for  $H \rightarrow W^+W^-$  with one or both  $W$  bosons decaying hadronically. These are the  $H \rightarrow W^+W^- \rightarrow \ell\nu q\bar{q}$  [19] and  $VH \rightarrow \ell\nu q\bar{q}q\bar{q}$  [12] analyses, both of which are much like the  $WH \rightarrow \ell\nu b\bar{b}$  search except that the jets are not  $b$ -tagged and the  $VH \rightarrow \ell\nu q\bar{q}q\bar{q}$  analysis requires at least four jets. The  $VH \rightarrow \ell\nu q\bar{q}q\bar{q}$  analysis represents the first search for the SM Higgs boson in this final state signature.

Finally, we include an analysis that searches for Higgs bosons decaying to two photons [16]. All three dominant production mechanisms, gluon-gluon fusion, vector boson fusion, and associated production, are considered in this search. The contribution of jets misidentified as photons is reduced by combining information sensitive to differences in the energy deposition from these particles in the tracker, calorimeter, and preshower in a neural network. The output of boosted decision trees, rather than the diphoton invariant mass, is used as the final discriminating variable. Relative to the previous result [26], improved vertexing and energy calibrations have been incorporated. Additionally, the impact of systematic uncertainties is now reduced by inclusion of photon-dominated and jet-dominated sub-channels in the limit setting procedure. The overall sensitivity improvement is approximately 30%.

For all analyses, the backgrounds from multijet production are measured in data. The other backgrounds were generated by PYTHIA [27], ALPGEN [28], SHERPA [29], or SINGLETOP [30], with PYTHIA providing parton-showering and hadronization. Drell-Yan,  $W$ , and diboson background cross sections are normalized either to next-to-leading order (NLO) calculations from MCFM [31] or, when possible, to data control samples. Top pair and single top production are normalized to approximate next-to-next-to-NLO [32] and next-to-next-to-NLO [33] calculations, respectively.

### III. SIGNAL PREDICTIONS AND UNCERTAINTIES

A common approach to the signal predictions and associated uncertainties is followed by both the CDF and DØ Collaborations. An outline of the procedures followed is given here; a more complete discussion can be found in Ref. [34].

The Monte Carlo signal simulation is provided by the leading-order (LO) generator PYTHIA (with CTEQ6L1 [35] LO parton distribution functions), which includes a parton shower and fragmentation and hadronization models. We reweight the Higgs boson  $p_T$  spectra in the PYTHIA Monte Carlo samples to that predicted by HQT [36] when making predictions of differential distributions of gluon-gluon fusion signal events. To evaluate the impact of the scale uncertainty on the differential spectra, we use the RESBOS [37] generator, and apply the scale-dependent differences in the Higgs boson  $p_T$  spectrum to the HQT prediction, and propagate these to our final discriminants as a systematic uncertainty on the shape of the final variable distribution, which is included in the calculation of the limits.

We normalize the Higgs boson signal predictions to the most recent higher-order calculations available. The  $gg \rightarrow H$  production cross section is calculated at next-to-next-to leading order (NNLO) in QCD with a next-to-next-to leading log (NNLL) resummation of soft gluons; the calculation also includes two-loop electroweak effects and handling of the running  $b$  quark mass [38, 39]. The numerical values in Table II are updates [40] of these predictions with  $m_t$  set to 173.1 GeV [41], and an exact treatment of the massive top and bottom loop corrections up to NLO + next-to-leading-log accuracy. The factorization and renormalization scale choice for this calculation is  $\mu_F = \mu_R = m_H$ . These calculations are refinements of the earlier NNLO calculations of the  $gg \rightarrow H$  production cross section [42–44]. Electroweak corrections were computed in Refs. [45, 46]. Soft gluon resummation was introduced in the prediction of the  $gg \rightarrow H$  production cross section [47]. The  $gg \rightarrow H$  production cross section depends strongly on the gluon parton density function, and the accompanying value of  $\alpha_s(q^2)$ . The cross sections used here are calculated with the MSTW 2008 NNLO PDF set [48], as recommended by the PDF4LHC working group [49]. The inclusive (over jet multiplicity) Higgs boson production cross sections are listed in Table II.

TABLE II: The production cross sections (in fb) and decay branching fractions (in %) for each SM Higgs boson mass (in GeV) assumed for the combination.

$m_H$	$\sigma_{gg \rightarrow H}$	$\sigma_{WH}$	$\sigma_{ZH}$	$\sigma_{VBF}$	$B(H \rightarrow b\bar{b})$	$B(H \rightarrow c\bar{c})$	$B(H \rightarrow \tau^+\tau^-)$	$B(H \rightarrow W^+W^-)$	$B(H \rightarrow ZZ)$	$B(H \rightarrow \gamma\gamma)$
100	1821.8	281.10	162.7	100.1	79.1	3.68	8.36	1.11	0.113	0.159
105	1584.7	238.70	139.5	92.3	77.3	3.59	8.25	2.43	0.215	0.178
110	1385.0	203.70	120.2	85.1	74.5	3.46	8.03	4.82	0.439	0.197
115	1215.9	174.50	103.9	78.6	70.5	3.27	7.65	8.67	0.873	0.213
120	1072.3	150.10	90.2	72.7	64.9	3.01	7.11	14.3	1.60	0.225
125	949.3	129.50	78.5	67.1	57.8	2.68	6.37	21.6	2.67	0.230
130	842.9	112.00	68.5	62.1	49.4	2.29	5.49	30.5	4.02	0.226
135	750.8	97.20	60.0	57.5	40.4	1.87	4.52	40.3	5.51	0.214
140	670.6	84.60	52.7	53.2	31.4	1.46	3.54	50.4	6.92	0.194
145	600.6	73.70	46.3	49.4	23.1	1.07	2.62	60.3	7.96	0.168
150	539.1	64.40	40.8	45.8	15.7	0.725	1.79	69.9	8.28	0.137
155	484.0	56.20	35.9	42.4	9.18	0.425	1.06	79.6	7.36	0.100
160	432.3	48.50	31.4	39.4	3.44	0.159	0.397	90.9	4.16	0.0533
165	383.7	43.60	28.4	36.6	1.19	0.0549	0.138	96.0	2.22	0.0230
170	344.0	38.50	25.3	34.0	0.787	0.0364	0.0920	96.5	2.36	0.0158
175	309.7	34.00	22.5	31.6	0.612	0.0283	0.0719	95.8	3.23	0.0123
180	279.2	30.10	20.0	29.4	0.497	0.0230	0.0587	93.2	6.02	0.0102
185	252.1	26.90	17.9	27.3	0.385	0.0178	0.0457	84.4	15.0	0.00809
190	228.0	24.00	16.1	25.4	0.315	0.0146	0.0376	78.6	20.9	0.00674
195	207.2	21.40	14.4	23.7	0.270	0.0125	0.0324	75.7	23.9	0.00589
200	189.1	19.10	13.0	22.0	0.238	0.0110	0.0287	74.1	25.6	0.00526

For analyses that consider inclusive  $gg \rightarrow H$  production, but do not split the signal prediction into separate channels based on the number of reconstructed jets, we use the inclusive uncertainties from the simultaneous variation of the factorization and renormalization scales up and down by a factor of two. We use the prescription of the PDF4LHC working group for evaluating PDF uncertainties on the inclusive production cross section. QCD scale uncertainties that affect the cross section via their impact on the PDFs are included as a correlated part of the total scale uncertainty. The remainder of the PDF uncertainty is treated as uncorrelated with the QCD scale uncertainty.

For analyses seeking  $gg \rightarrow H$  production that divide events into categories based on the number of reconstructed jets, we employ an approach for evaluating the impact of the scale uncertainties following Ref. [50]. We treat the QCD scale uncertainties obtained from the NNLL inclusive [38, 39], NLO with one or more jets [51], and NLO with two or more jets [52] cross section calculations as uncorrelated with one another. We then obtain QCD scale uncertainties for the exclusive  $gg \rightarrow H + 0$  jet, 1 jet, and 2 or more jet categories by propagating the uncertainties on the inclusive cross section predictions through the subtractions needed to predict the exclusive rates. For example, the  $H+0$  jet cross section is obtained by subtracting the NLO  $H + 1$  or more jet cross section from the inclusive NNLL+NNLO cross section. Therefore, we assign three separate, uncorrelated scale uncertainties which lead to correlated and anticorrelated uncertainty contributions between exclusive jet categories. The procedure in Ref. [51] is used to determine PDF model uncertainties. These are obtained separately for each jet bin and treated as 100% correlated between jet bins.

Another source of uncertainty in the prediction of  $\sigma(gg \rightarrow H)$  is the extrapolation of the QCD corrections computed for the heavy top quark loops to the light-quark loops included as part of the electroweak corrections. It has been argued [38] that the factorization of QCD corrections is known to work well for Higgs boson masses much larger than the masses of the particles contributing to the loop. A 4% change in the predicted cross section is seen when all QCD corrections are removed from the diagrams containing light-flavored quark loops, which would represent an overestimate of the uncertainty. For the  $b$  quark loop [38], the QCD corrections are much smaller than for the top loop, further giving confidence that it does not introduce large uncertainties. Uncertainties at the level of 1-2% due to these effects are included in the predictions we use [38, 39].

We consider all significant Higgs boson production modes in our searches. Besides gluon-gluon fusion through virtual quark loops, we consider Higgs boson production in association with a  $W$  or  $Z$  vector boson, and vector boson fusion. We use the  $WH$  and  $ZH$  production cross sections computed at NNLO [53]. This calculation starts with the NLO calculation of v2HV [54] and includes NNLO QCD contributions [55], as well as one-loop electroweak corrections [56]. We use the vector-boson fusion cross section computed at NNLO in QCD [57]. Electroweak corrections to the vector-boson fusion production cross section are computed with the HAWK program [58], and are very small (0.03 fb and

less) for the Higgs boson mass range considered here.

The Higgs boson decay branching ratio predictions are calculated with HDECAY [59], and are also listed in Table II. We use HDECAY Version 3.53. While the  $HWW$  coupling is well predicted,  $B(H \rightarrow W^+W^-)$  depends on the partial widths of all other Higgs boson decays. The partial width  $\Gamma(H \rightarrow b\bar{b})$  is sensitive to  $m_b$  and  $\alpha_s$ ,  $\Gamma(H \rightarrow c\bar{c})$  is sensitive to  $m_c$  and  $\alpha_s$ , and  $\Gamma(H \rightarrow gg)$  is sensitive to  $\alpha_s$ . The impacts of these uncertainties on  $B(H \rightarrow W^+W^-)$  depend on  $m_H$  due to the fact that  $B(H \rightarrow b\bar{b})$ ,  $B(H \rightarrow c\bar{c})$ ,  $B(H \rightarrow gg)$  become very small for Higgs boson masses above 160 GeV, while they have a larger impact for lower  $m_H$ . We use the uncertainties on the branching fraction  $B(H \rightarrow W^+W^-)$  from Ref. [60]. At  $m_H = 130$  GeV, for example, the  $m_b$  variation gives a  ${}_{+1.70}^{-4.89}\%$  relative variation in  $B(H \rightarrow W^+W^-)$ ,  $\alpha_s$  gives a  ${}_{+1.09}^{-1.02}\%$  variation, and  $m_c$  gives a  ${}_{+0.51}^{-0.45}\%$  variation. At  $m_H = 165$  GeV, all three of these uncertainties drop below 0.1%.

#### IV. LIMIT CALCULATIONS

We combine results using the  $CL_s$  method with a negative log-likelihood ratio (LLR) test statistic [61]. The value of  $CL_s$  is defined as  $CL_s = CL_{s+b}/CL_b$  where  $CL_{s+b}$  and  $CL_b$  are the confidence levels for the signal-plus-background hypothesis and the background-only hypothesis, respectively. These confidence levels are evaluated by integrating corresponding LLR distributions populated by simulating outcomes via Poisson statistics. Separate channels and bins are combined by summing LLR values over all bins and channels. This method provides a robust means of combining individual channels while maintaining individual channel sensitivities and incorporating systematic uncertainties. Systematic uncertainties are treated as Gaussian uncertainties on the expected number of signal and background events, not the outcomes of the limit calculations. This approach ensures that the uncertainties and their correlations are propagated to the outcome with their proper weights. The  $CL_s$  approach used in this combination utilizes binned final-variable distributions rather than a single-bin (fully integrated) value for each contributing analysis. The exclusion criteria are determined by increasing the signal cross section until  $CL_s = 1 - \alpha$ , which defines a signal cross section excluded at 95% confidence level for  $\alpha = 0.95$ .

##### A. Final Variable Distributions

Searches are performed assuming different values of the Higgs boson mass between 100 GeV and 200 GeV, in steps of 5 GeV. For each tested Higgs boson mass, each analysis provides binned distributions of the final discriminants for each sub-channel. These input distributions can be found in the corresponding references (see Table I). The limit calculation uses the individual inputs, however, for visualization purposes, it can be useful to collect all of the inputs into a single distribution. To preserve the sensitivity from the bins with high signal-to-background ( $s/b$ ) ratios, only bins with similar  $s/b$  are combined. Therefore, the aggregate distribution is made by reordering all of the bins from the input distributions according to  $s/b$ . The range of  $s/b$  is quite large, so  $\log_{10}(s/b)$  is used. Figure 1 shows the aggregate distributions for test Higgs boson masses of 115 GeV, 125 GeV, and 165 GeV, indicating good agreement between data and predictions over many orders of magnitude. Figure 2 shows the same distributions after subtracting the expected background from the data. Integrating the distributions in Fig. 1 from *right to left* (*i.e.*, starting with the highest  $s/b$  events) allows one to see how the data compare to the background-only and signal+background hypotheses as the most significant events are accumulated. Figure 3 shows these cumulative distributions for the  $\approx 150$  most significant events as a function of the integrated number of predicted signal events. For a Higgs boson mass of 125 GeV, the highest  $s/b$  bins contain an excess of signal like candidate events, while for a mass of 165 GeV, the data clearly follow the background-only expectation.

##### B. Systematic Uncertainties

The systematic uncertainties differ between analyses for both the signals and backgrounds [10–20]. Here we summarize only the largest contributions. Most analyses carry an uncertainty on the integrated luminosity of 6.1% [62], while the overall normalization of other analyses is determined from the NNLO  $Z/\gamma^*$  cross section in data events near the peak of  $Z \rightarrow \ell\ell$  decays. The  $H \rightarrow b\bar{b}$  analyses have an uncertainty on the  $b$ -tagging rate of 1-10%. These

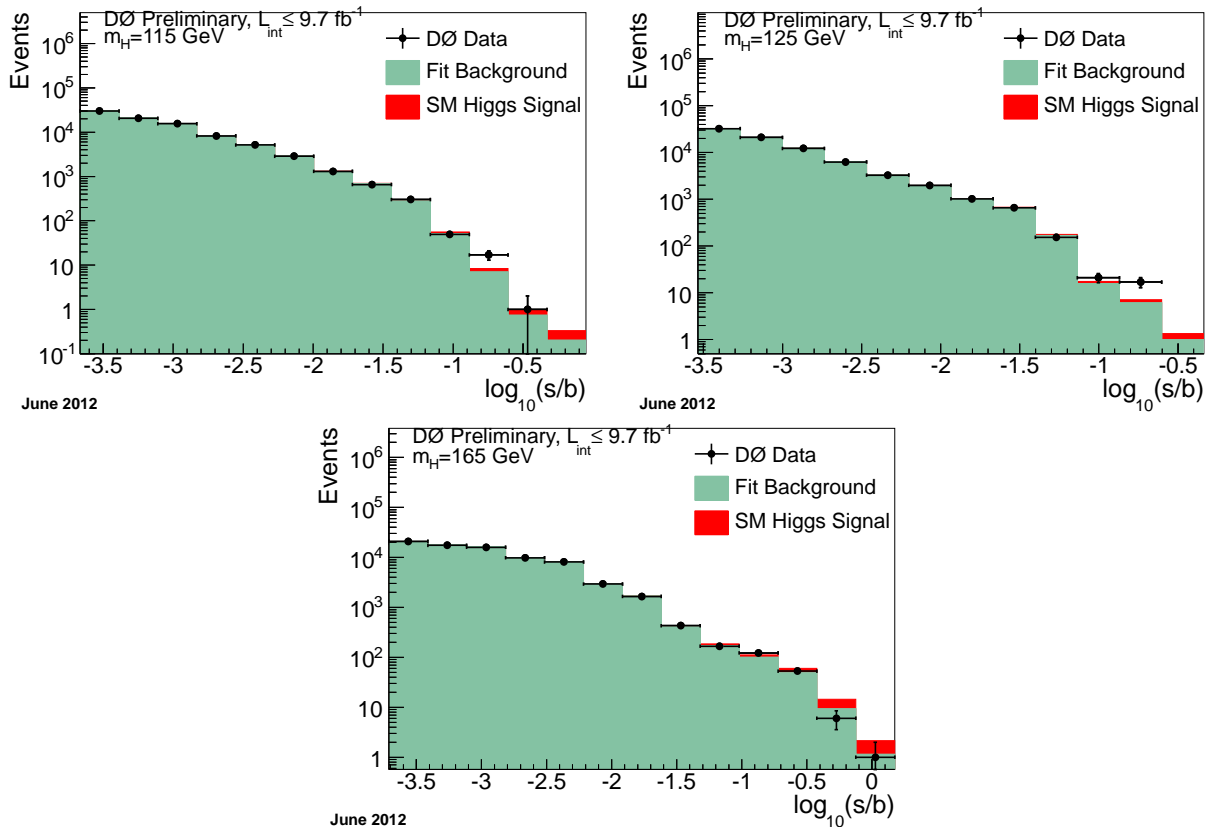


FIG. 1: Distributions of  $\log_{10}(s/b)$  for the data from all contributing channels for Higgs boson masses of 115 GeV, 125 GeV, and 165 GeV. The data are shown with points and the expected signal is shown stacked on top of the backgrounds. Only statistical uncertainties on the data points are shown. Systematic uncertainties on the background prediction are displayed in Fig. 2.

analyses also have an uncertainty on the jet measurement and acceptances of  $\sim 7\%$ . All analyses include uncertainties associated with lepton measurement and acceptances, which range from 1-9% depending on the final state. The largest contribution for all analyses is the uncertainty on the background cross sections at 4-30% depending on the analysis channel and specific background. These values include both the uncertainty on the theoretical cross section calculations and the uncertainties on the higher-order correction factors. The uncertainty on the expected multijet background is dominated by the statistics of the data sample from which it is estimated, and is considered separately from the other cross section uncertainties. All analyses take into account the uncertainties on the theoretical production cross sections for the different signal processes due to PDF model and scale choice. The  $H \rightarrow W^+W^- \rightarrow \ell^+\nu\ell^-\nu$  ( $\ell = e, \mu$ ) analyses divide the data by jet multiplicity and, as discussed, apply different uncertainties on the gluon-gluon fusion Higgs boson production cross section for each jet multiplicity final state. In addition, several analyses incorporate uncertainties that alter the differential distributions and kinematics of the dominant backgrounds in the analyses. These shapes are derived from the potential variations of the final variables due to generator and background modeling uncertainties. Further details on the systematic uncertainties are given in Appendix A.

In much of the phase space, the systematic uncertainties for background rates are several times larger than the signal expectation itself and are an important factor in the calculation of limits. Each systematic uncertainty is folded into the signal and background expectations in the limit calculation via Gaussian distributions. These Gaussian values are sampled for each Monte Carlo (MC) trial (pseudo-experiment) using Poisson distributions for the number of signal and background events. Several of the systematic uncertainties, for example the jet energy scale uncertainty, typically impact the shape of the final variable. These variations in the final variable distributions were preserved in the description of systematic fluctuations for each Poisson trial. Correlations between systematic sources are carried through in the calculation. For example, the uncertainty on the integrated luminosity is held to be correlated between all signals and backgrounds and, thus, the same fluctuation in the luminosity is common to all channels for a single pseudo-experiment. All systematic uncertainties originating from a common source are held to be correlated, as detailed in Table III.

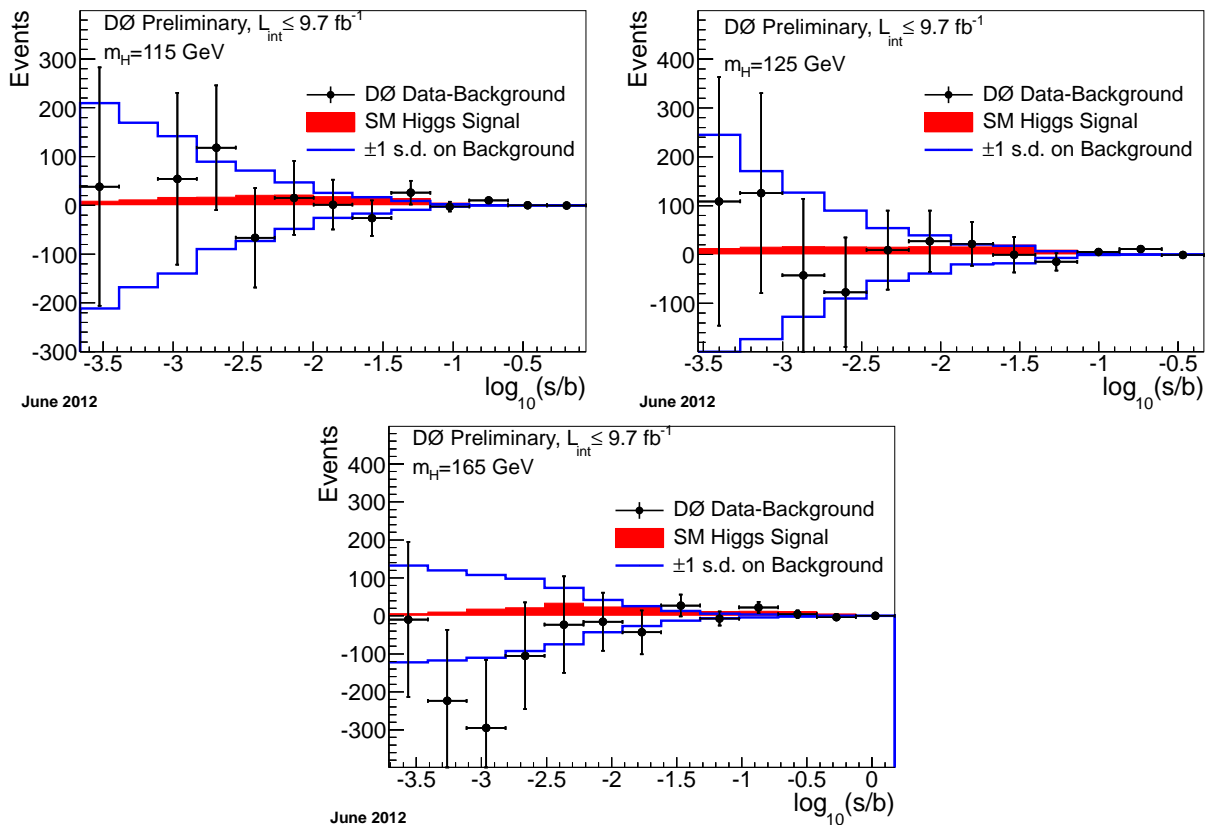


FIG. 2: Background subtracted distributions of  $\log_{10}(s/b)$  for the data from all contributing channels for Higgs boson masses of 115 GeV, 125 GeV, and 165 GeV. The background subtracted data are shown as points and the expected signal is the red histogram. The blue lines indicate the uncertainty on the background prediction.

To minimize the degrading effects of systematic uncertainties on the search sensitivity, the individual background contributions are fitted to the data observation by maximizing a likelihood function for each hypothesis [63]. The likelihood is a joint Poisson probability over the number of bins in the calculation and is a function of the nuisance parameters in the system and their associated uncertainties, which are given an additional Gaussian constraint associated with their prior predictions. The maximization of the likelihood function is performed over the nuisance parameters. A fit is performed to both the background-only (b) and signal-plus-background (s+b) hypothesis separately for each Poisson MC trial.

## V. RESULTS

We derive limits on SM Higgs boson production  $\sigma \times BR(H \rightarrow b\bar{b}/W^+W^-/\tau^+\tau^-/\gamma\gamma)$  via individual channels [10–20]. The relative contributions of the different production and decay modes are set to the SM prediction. To facilitate model transparency and to accommodate analyses with different degrees of sensitivity, we present our results in terms of the ratio of 95% C.L. upper cross section limits to the SM predicted cross section as a function of Higgs boson mass. The SM prediction for Higgs boson production would therefore be considered excluded at 95% C.L. when this limit ratio falls below unity.

The individual analyses described in Table I are grouped to evaluate combined limits over the range  $100 \leq m_H \leq 200$  GeV. The  $ZH \rightarrow \ell\ell b\bar{b}$ ,  $ZH \rightarrow \nu\bar{\nu} b\bar{b}$ ,  $WH \rightarrow \ell\nu b\bar{b}$  and  $H \rightarrow \gamma\gamma$  analyses contribute for  $m_H \leq 150$  GeV, the  $VH \rightarrow ee\mu/\mu\mu e+X$ ,  $VH \rightarrow \tau\tau\mu+X$  and  $VH \rightarrow \ell\nu q\bar{q}q\bar{q}$  analyses contribute for  $m_H \geq 100$  GeV, the  $VH \rightarrow e^\pm\mu^\pm+X$  and  $H \rightarrow W^+W^- \rightarrow (ee, \mu\mu, e\mu)\nu\nu$  analyses contribute for  $m_H \geq 115$  GeV, and the  $H \rightarrow W^+W^- \rightarrow \ell\nu q\bar{q}$  analysis contributes for  $m_H \geq 155$  GeV.



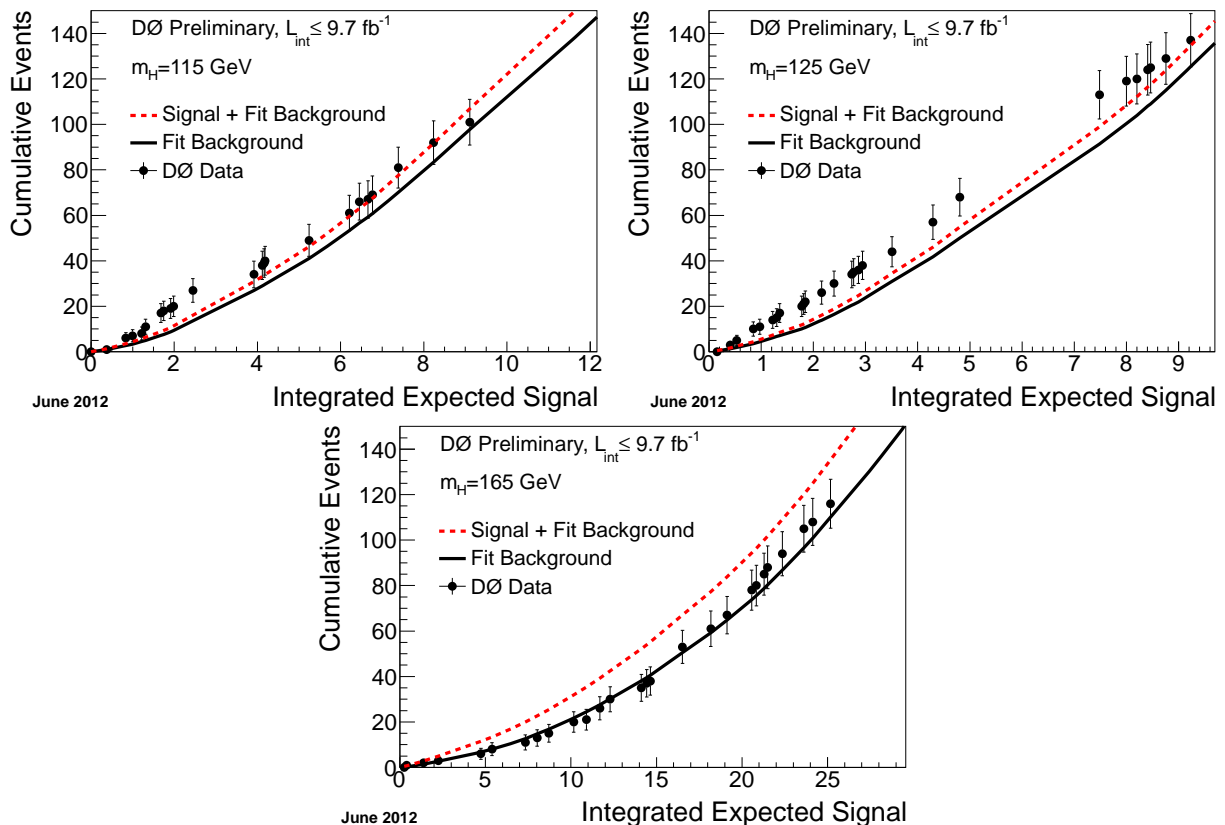


FIG. 3: Cumulative number of events for the highest  $s/b$  bins from all contributing channels for Higgs boson masses of 115 GeV, 125 GeV, and 165 GeV. The integrated background-only and signal+background predictions are shown as a function of the accumulated number of signal events. The points show the integrated number of observed events, including only the statistical uncertainty, which is correlated point-to-point. Systematic uncertainties on the integrated background-only and signal+background predictions are not displayed.

Figure 4 shows the expected and observed 95% C.L. cross section limits as a ratio to the SM cross section and for the probed mass region ( $100 \leq m_H \leq 200$  GeV), with all analyses combined. These results are also summarized in Table IV. The LLR distributions for the full combination are shown in Fig. 5. Included in these figures are the median LLR values for the signal-plus-background hypothesis ( $LLR_{s+b}$ ), background-only hypothesis ( $LLR_b$ ), and the observed data ( $LLR_{obs}$ ). The shaded bands represent the 1 and 2 standard deviation ( $\sigma$ ) departures for  $LLR_b$ . These distributions can be interpreted as follows:

- The separation between  $LLR_b$  and  $LLR_{s+b}$  provides a measure of the discriminating power of the search. This is the ability of the analysis to separate the  $s + b$  and  $b$ -only hypotheses.
- The width of the  $LLR_b$  distribution (shown here as one and two standard deviation ( $\sigma$ ) bands) provides an estimate of how sensitive the analysis is to a signal-like background fluctuation in the data, taking account of the presence of systematic uncertainties. For example, the analysis sensitivity is limited when a  $1\sigma$  background fluctuation is large compared to the signal expectation.
- The value of  $LLR_{obs}$  relative to  $LLR_{s+b}$  and  $LLR_b$  indicates whether the data distribution appears to be more like signal-plus-background or background-only. As noted above, the significance of any departures of  $LLR_{obs}$  from  $LLR_b$  can be evaluated by the width of the  $LLR_b$  distribution.

Figure 6 illustrates the exclusion criterion  $1 - CL_s$  for the region  $100 \leq m_H \leq 200$  GeV. We provide in Fig. 7 the values for the observed  $CL_{s+b}$  and its expected distribution as a function of  $m_H$ . The quantity  $CL_{s+b}$  is the  $p$ -value for the signal-plus-background hypothesis. Figure 8 contains the values for the observed  $1 - CL_b$ , which is the  $p$ -value for the background-only hypothesis. These probabilities are local  $p$ -values, corresponding to searches for each value of

TABLE III: The correlation matrix for the analysis channels. All uncertainties within a group are considered 100% correlated across channels. The correlated systematic uncertainty on the background cross section ( $\sigma$ ) is itself subdivided according to the different background processes in each analysis.

Source	$WH \rightarrow \ell\nu b\bar{b}$	$ZH \rightarrow \nu\bar{\nu} b\bar{b}$	$ZH \rightarrow \ell\ell b\bar{b}$	$H \rightarrow W^+W^- \rightarrow \ell^\pm\nu\ell^\mp\nu$
Luminosity	×	×		
Jet Energy Scale	×	×	×	×
Jet ID	×	×	×	×
Tau Energy Scale/ID				
Electron ID/Trigger	×	×	×	×
Muon ID/Trigger	×	×	×	×
Photon ID/Trigger				
$b$ Jet Tagging	×	×	×	
Background $\sigma$	×	×	×	×
Background Modeling				
Multijet				
Signal $\sigma$	×	×	×	×
Signal modeling				×

Source	$VH \rightarrow VWW$	$VH \rightarrow \ell\nu q\bar{q}q\bar{q}$	$H \rightarrow W^+W^- \rightarrow \ell\nu q\bar{q}$	$H+X \rightarrow \mu^\pm\tau_{had}^\mp + \leq 1j$	$H \rightarrow \gamma\gamma$
Luminosity		×	×	×	×
Jet Energy Scale	×	×	×	×	
Jet ID	×	×	×	×	
Tau Energy Scale/ID				×	
Electron ID/Trigger	×	×	×	×	
Muon ID/Trigger	×	×	×	×	
Photon ID/Trigger					×
$b$ Jet Tagging					
Background $\sigma$	×	×	×	×	
Background Modeling					
Multijet					
Signal $\sigma$	×	×	×	×	×
Signal modeling	×	×	×	×	×

$m_H$  separately, thus they do not include the look-elsewhere-effect (LEE). These two  $p$ -values ( $CL_{s+b}$  and  $1-CL_b$ ) each provide information on the compatibility of their respective hypothesis with the observed data. Small values indicate rejection of the hypothesis and values near unity indicate general agreement between the hypothesis in question and the data. As can be seen in Figure 7, the observed value of  $CL_{s+b}$  drops to  $\approx 1\%$  for Higgs boson masses near 160 GeV, indicating very small compatibility with the signal-plus-background hypothesis in this mass range. In contrast, the observed value of  $CL_{s+b}$  is close to 0.5 for  $120 \text{ GeV} \leq m_H \leq 140 \text{ GeV}$ , favoring the hypothesis of a signal in that mass range. At  $m_H = 135$  (120) GeV, the local  $p$ -value of  $1-CL_b$  is 2.4% (2.8%), corresponding to 2.0 (1.9) Gaussian standard deviations above the background-only prediction.

We estimate the LEE effect as discussed below (see Ref. [34] for more details). In the mass range 100–135 GeV, where the low-mass  $H \rightarrow b\bar{b}$  searches dominate, the reconstructed mass resolution is 10–15%. We therefore estimate a trials factor of approximately two for the low-mass region. For the high-mass searches, the  $H \rightarrow W^+W^-$  searches dominate the sensitivity. There is little-to-no resolution in reconstructing  $m_H$  in these channels due to the presence of two neutrinos in the final state of the most sensitive analyses. We expect a trials factor of approximately two for the high-mass searches. In total, we expect that there are roughly four possible independent locations for uncorrelated excesses to appear in our analysis. The global  $p$ -value is therefore  $1 - (1 - p_{\min})^4$ , using the Dunn-Šidák correction [64], where  $p_{\min}$  is the smallest local  $p$ -value found as a function of  $m_H$ . The global significance for such an excess anywhere in the full mass range is estimated to be approximately 1.3 standard deviations.

As a further investigation of this deviation from the background-only hypothesis, we present in Figure 9 the distribution of the best-fit Higgs boson signal cross section ratio to the SM prediction ( $\sigma^{\text{Fit}}/\sigma^{\text{SM}}$ ). This value is obtained by performing a maximum likelihood fit over all search channels simultaneously, in which the fit is allowed to vary all nuisance parameters within their priors and with the Higgs boson signal rate as a free parameter. The result of this fit, shown along with the  $\pm 1$  standard deviation distribution from the fit, yields a best-fit signal rate of roughly 1.5 times the SM Higgs boson predicted cross section for masses between 120 GeV and 140 GeV. And as

TABLE IV: Combined 95% C.L. expected (median) and observed limits on  $\sigma \times BR(H \rightarrow X)$  for SM Higgs boson production. The limits are reported in units of the SM production cross section times branching fraction.

$m_H$	100	105	110	115	120	125	130	135	140	145	150	155	160	165	170	175	180	185	190	195	200
Expected:	1.14	1.24	1.37	1.46	1.61	1.70	1.74	1.67	1.56	1.39	1.23	1.07	0.78	0.72	0.90	1.06	1.28	1.62	1.98	2.31	2.62
Observed:	1.04	1.52	1.39	2.11	2.84	2.94	3.10	3.14	2.83	2.05	1.57	1.39	0.84	0.73	0.98	1.57	1.59	1.95	2.59	3.22	4.38

expected from Figs 4-8, there is also an excursion from zero cross section near  $m_H = 200$  GeV. However, the excursion from the background hypothesis at  $m_H = 200$  GeV has a shape incompatible with that expected from a SM Higgs signal given the mass resolution, and is less significant than the excess between 120 GeV and 140 GeV, so it will not be discussed further in the following. We also explore the compatibility of the excess with the presence of a signal. Fig. 10 compares the LLR obtained from the data to the expectation from the signal+background hypothesis for  $m_H = 125$  GeV, at the rate predicted by the SM, and at the best fit signal rate. This test produces a broad negative excursion in the LLR that is similar to the observation in the data.

The low mass excesses can be studied by separating the contributing sources by Higgs boson decay:  $H \rightarrow b\bar{b}$  and  $H \rightarrow W^+W^-$ . Figures 11 and 13 show the LLR value for  $H \rightarrow b\bar{b}$  and  $H \rightarrow W^+W^-$  final states, respectively. Figure 11 includes contributions from  $ZH \rightarrow \ell\ell b\bar{b}$ ,  $ZH \rightarrow \nu\nu b\bar{b}$  and  $WH \rightarrow \ell\nu b\bar{b}$  searches, and illustrates a small data excess ( $\sim 1$  standard deviation above expected background) that is nonetheless compatible with the SM Higgs boson rate for  $120 \leq m_H \leq 135$  GeV. Figure 13 includes contributions from  $H \rightarrow W^+W^- \rightarrow \ell\nu\ell\nu$ ,  $H \rightarrow W^+W^- \rightarrow \ell\nu jj$  and  $VH \rightarrow W^+W^-/ZZ$  searches, and shows a general excess of data somewhat larger than the background prediction for  $m_H \leq 140$  GeV. Figures 12 and 14 show the expected and observed 95% C.L. cross section limits as a ratio to the SM cross section for the probed mass region for  $H \rightarrow b\bar{b}$  and  $H \rightarrow W^+W^-$  final states, respectively.

Appendix B presents a comparison between the results documented in this note and the previous results [8]. In general both sets of results are found to be consistent given the improvements to sensitivity in the various contributing analyses.

## VI. CONCLUSIONS

We have presented a combination of searches for the standard model Higgs boson at the DØ experiment using the full Run II data set of  $9.7 \text{ fb}^{-1}$  of  $p\bar{p}$  collisions at  $\sqrt{s} = 1.96$  TeV. These searches are carried out for Higgs boson masses ( $m_H$ ) in the range  $100 \leq m_H \leq 200$  GeV. In most of the searched region, no significant departure of the data from the background estimation is found, and upper limits on the standard model Higgs boson production cross section are derived as a function of  $m_H$ . The observed 95% C.L. upper limits are found to be a factor of 2.11 (0.73) times the predicted standard model cross section at  $m_H = 115$  (165) GeV, while the expected limit is found to be a factor of 1.46 (0.72) times the standard model prediction for the same mass(es). We exclude at the 95% C.L. the region  $159 < m_H < 170$  GeV with an *a priori* expected exclusion of  $156 < m_H < 173$  GeV. In the mass range 120–140 GeV, the data exhibit an excess above the background prediction with a local significance of approximately two Gaussian standard deviations. The results presented here supersede the previous DØ combination results [8].

## Acknowledgments

We thank the staffs at Fermilab and collaborating institutions, and acknowledge support from the DOE and NSF (USA); CEA and CNRS/IN2P3 (France); MON, Rosatom and RFBR (Russia); CNPq, FAPERJ, FAPESP and FUNDUNESP (Brazil); DAE and DST (India); Colciencias (Colombia); CONACyT (Mexico); NRF (Korea); FOM (The Netherlands); STFC and the Royal Society (United Kingdom); MSMT and GACR (Czech Republic); BMBF and DFG (Germany); SFI (Ireland); The Swedish Research Council (Sweden); and CAS and CNSF (China).

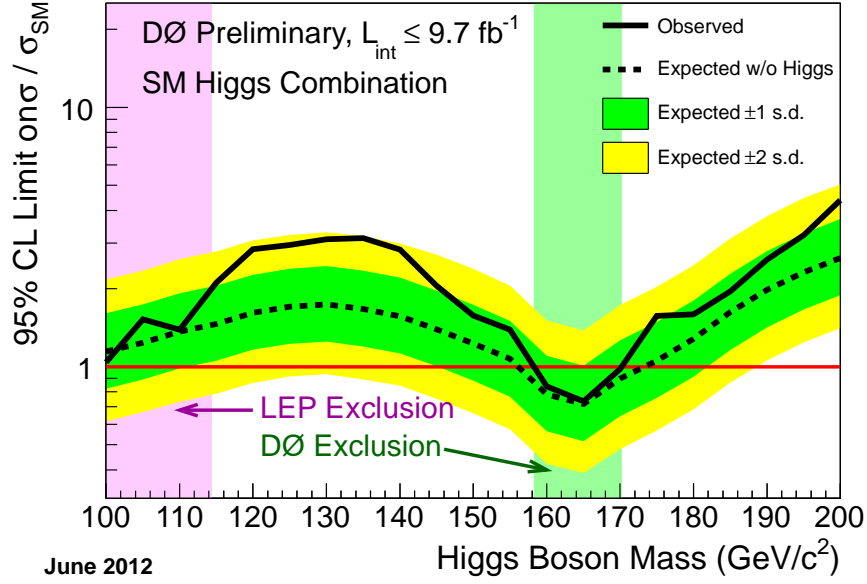


FIG. 4: Expected (median) and observed 95% C.L. cross section upper limit ratios for the combined  $WH/ZH/H, H \rightarrow b\bar{b}/W^+W^-/\gamma\gamma/\tau^+\tau^-$  analyses over the  $100 \leq m_H \leq 200$  GeV mass range. The green and yellow bands correspond to the regions enclosing 1 and 2 standard deviation fluctuations of the background, respectively.

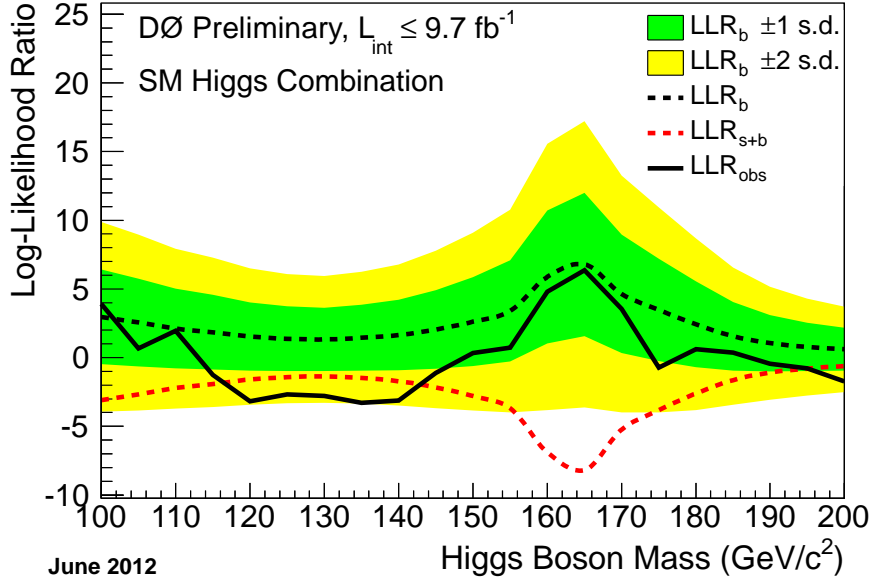


FIG. 5: Log-likelihood ratio distribution for the combined  $WH/ZH/H, H \rightarrow b\bar{b}/W^+W^-/\gamma\gamma/\tau^+\tau^-$  analyses over the  $100 \leq m_H \leq 200$  GeV mass range. The green and yellow bands correspond to the regions enclosing 1 and 2 standard deviation fluctuations of the background, respectively.

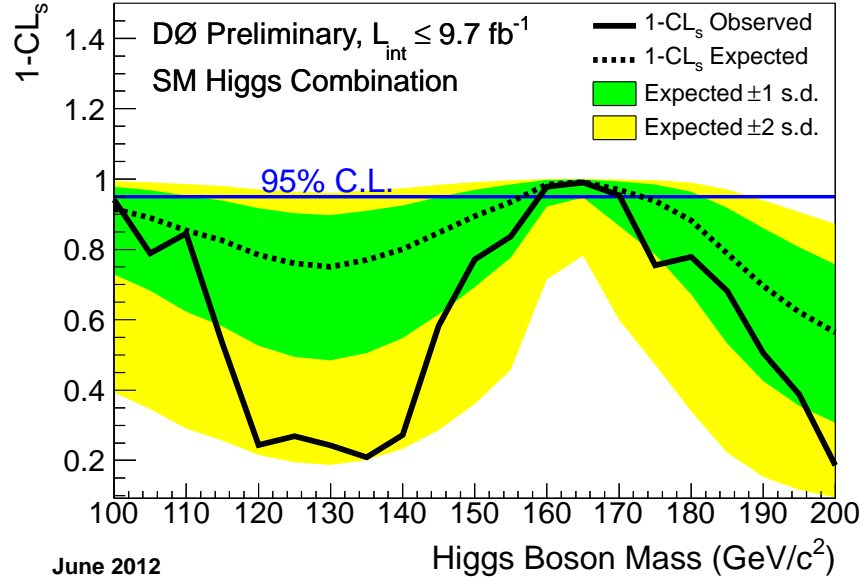


FIG. 6: The  $1 - CL_S$  (exclusion probability) distribution for the combined  $WH/ZH/H, H \rightarrow b\bar{b}/W^+W^-/\gamma\gamma/\tau^+\tau^-$  analyses over the  $100 \leq m_H \leq 200$  GeV mass range. The green and yellow bands correspond to the regions enclosing 1 and 2 standard deviation fluctuations of the background, respectively.

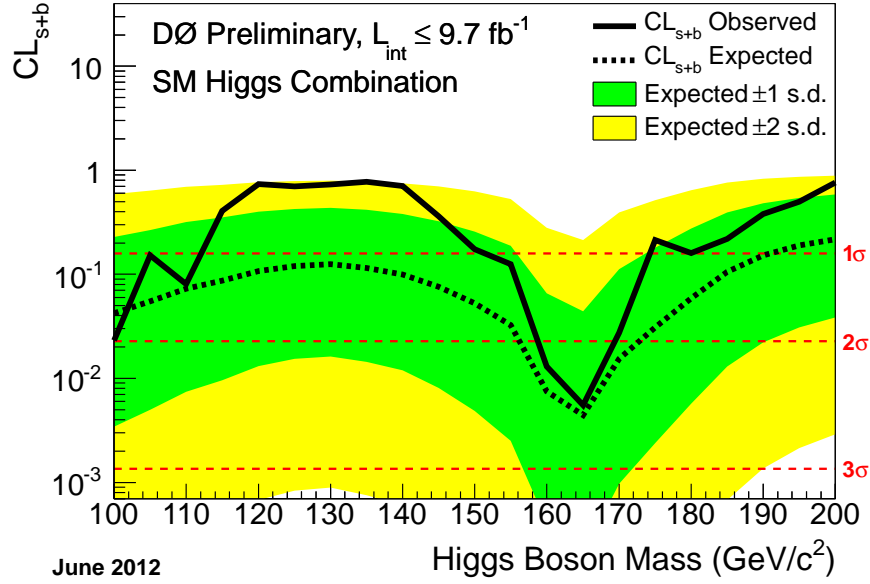


FIG. 7: The  $CL_{s+b}$  (signal-plus-background  $p$ -value) distribution for the combined  $WH/ZH/H, H \rightarrow b\bar{b}/W^+W^-/\gamma\gamma/\tau^+\tau^-$  analyses over the  $100 \leq m_H \leq 200$  GeV mass range. The green and yellow bands correspond to the regions enclosing 1 and 2 standard deviation fluctuations of the background, respectively. The three horizontal dashed lines indicate the  $p$ -values corresponding to significances of 1, 2 and 3 standard deviations.

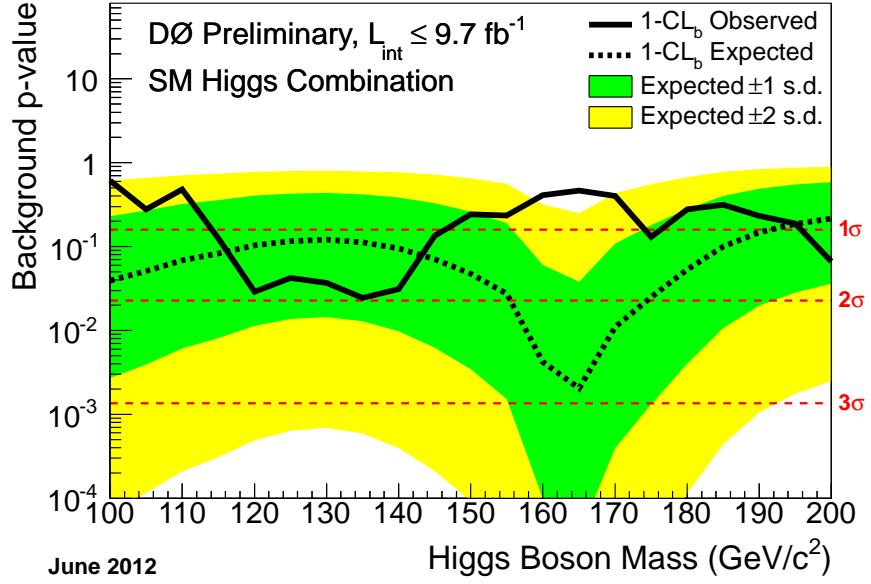


FIG. 8: The  $1 - CL_b$  (background  $p$ -value) distribution for the combined  $WH/ZH/H, H \rightarrow b\bar{b}/W^+W^-/\gamma\gamma/\tau^+\tau^-$  analyses over the  $100 \leq m_H \leq 200$  GeV mass range. Also shown is the expected background  $p$ -value for the SM Higgs boson signal (dotted line). The three horizontal dashed lines indicate the  $p$ -values corresponding to significances of 1, 2 and 3 standard deviations.

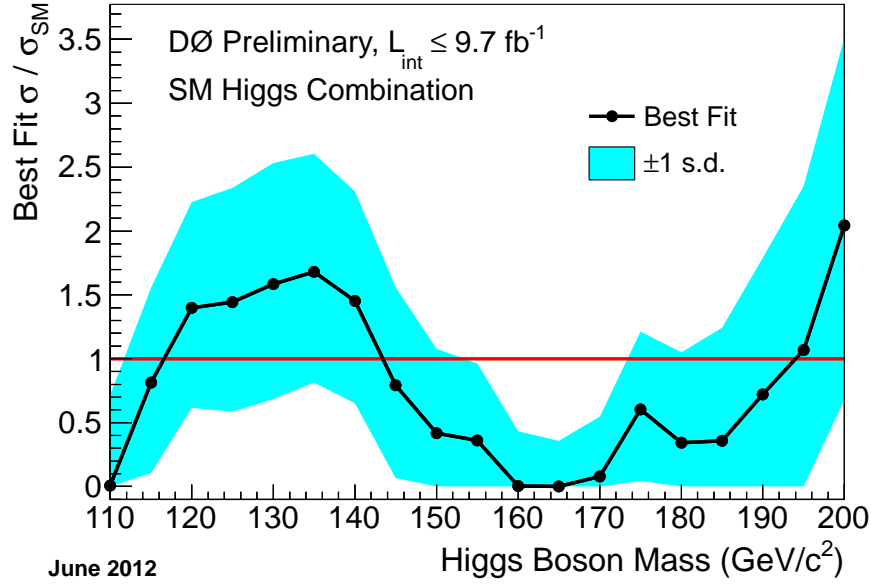


FIG. 9: The best-fit signal cross section ratio to the standard model Higgs boson prediction ( $\sigma^{Fit}/\sigma^{SM}$ ) for the combined  $WH/ZH/H, H \rightarrow b\bar{b}/W^+W^-/\gamma\gamma/\tau^+\tau^-$  analyses over the  $100 \leq m_H \leq 200$  GeV mass range. This value indicates the value of the Higgs boson cross section that would best match the observed data in a global fit over all nuisance parameters. The Higgs boson cross section is treated as a free parameter, bounded at zero. The light-blue band indicates the  $\pm 1$  standard deviation region from the fit.

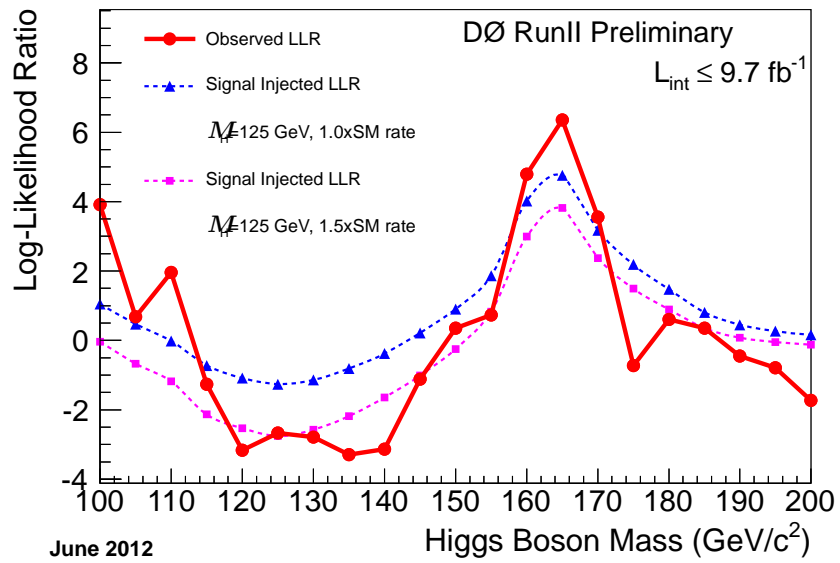


FIG. 10: Comparison of the LLR observed in the data with the LLR expected in the presence of a Higgs boson with a mass of 125 GeV at the rate predicted by the SM, and at a rate equal to 1.5 times the SM prediction.

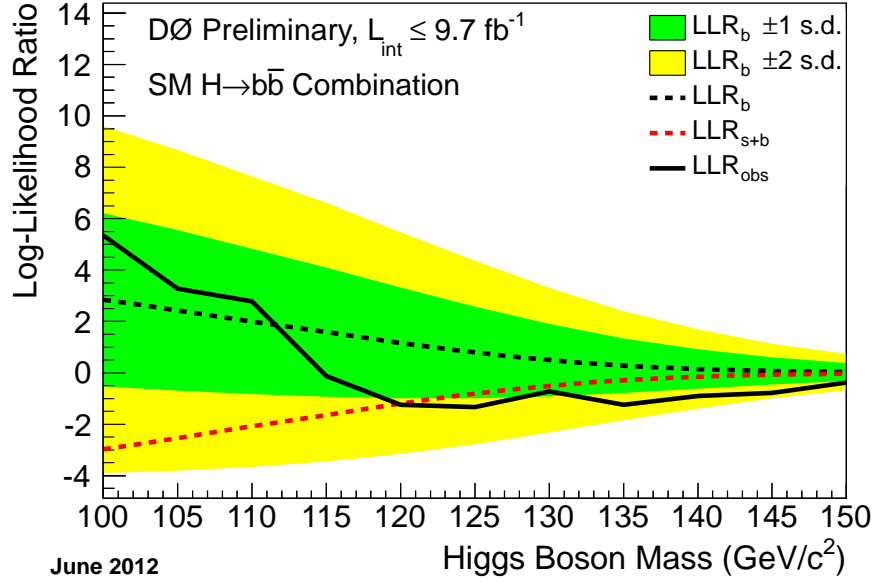


FIG. 11: Log-likelihood ratio distribution for the combined  $WH/ZH, H \rightarrow b\bar{b}$  analyses over the  $100 \leq m_H \leq 150$  GeV mass range. The green and yellow bands correspond to the regions enclosing 1 and 2 standard deviation fluctuations of the background, respectively.

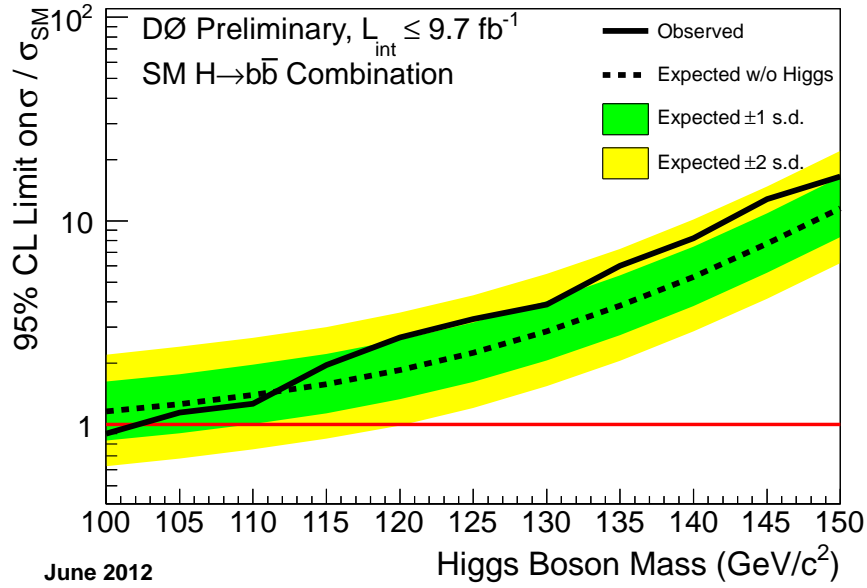


FIG. 12: Expected (median) and observed 95% C.L. cross section upper limit ratios for the combined  $WH/ZH, H \rightarrow b\bar{b}$  analyses over the  $100 \leq m_H \leq 150$  GeV mass range. The green and yellow bands correspond to the regions enclosing 1 and 2 standard deviation fluctuations of the background, respectively.

TABLE V: Expected (median) and observed 95% C.L. cross section upper limit ratios for the combined  $WH/ZH, H \rightarrow b\bar{b}$  analyses over the  $100 \leq m_H \leq 150$  GeV mass range.

$m_H$	100	105	110	115	120	125	130	135	140	145	150
Expected:	1.16	1.26	1.40	1.58	1.85	2.25	2.87	3.82	5.31	7.72	11.53
Observed:	0.90	1.14	1.26	1.96	2.67	3.30	3.89	6.01	8.23	12.81	16.52



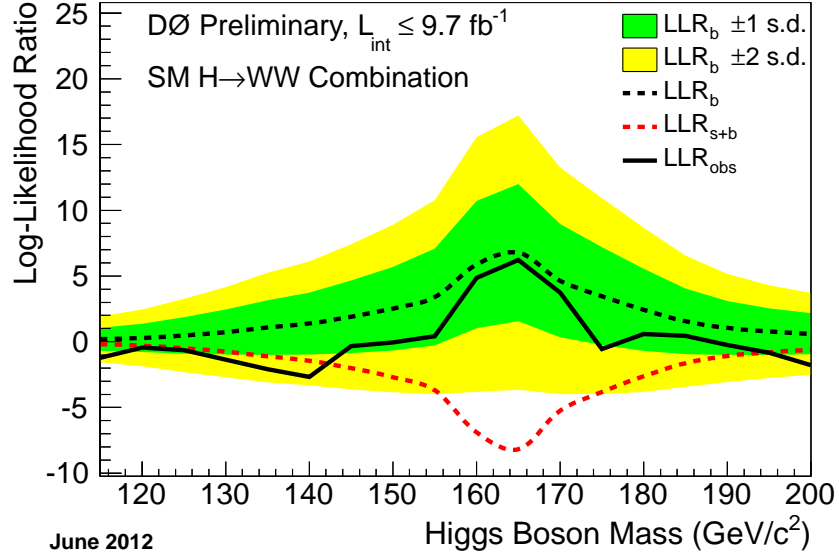


FIG. 13: Log-likelihood ratio distribution for the combined  $WH/ZH/H, H \rightarrow W^+W^-$  analyses over the  $115 \leq m_H \leq 200$  GeV mass range. The green and yellow bands correspond to the regions enclosing 1 and 2 standard deviation fluctuations of the background, respectively.

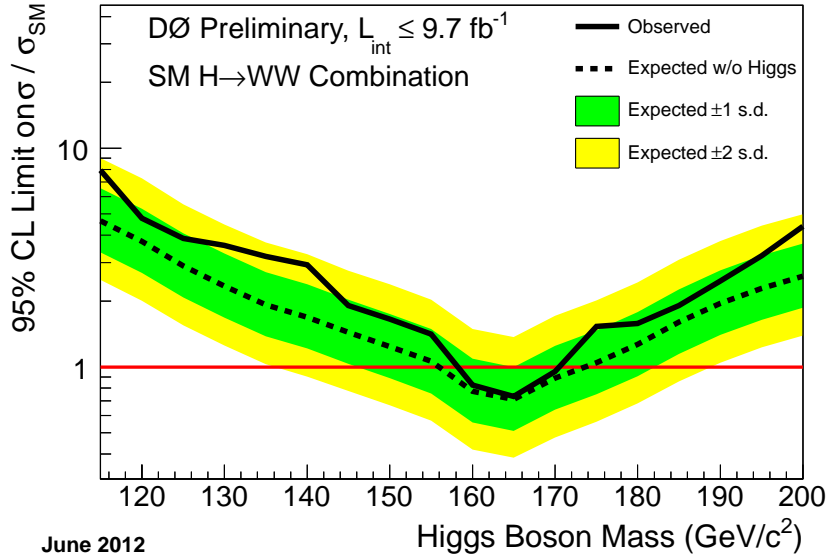


FIG. 14: Expected (median) and observed 95% C.L. cross section upper limit ratios for the combined  $WH/ZH/H, H \rightarrow W^+W^-$  analyses over the  $115 \leq m_H \leq 200$  GeV mass range. The green and yellow bands correspond to the regions enclosing 1 and 2 standard deviation fluctuations of the background, respectively.

TABLE VI: Expected (median) and observed 95% C.L. cross section upper limit ratios for the combined  $WH/ZH/H, H \rightarrow W^+W^-$  analyses over the  $115 \leq m_H \leq 200$  GeV mass range.

$m_H$	115	120	125	130	135	140	145	150	155	160	165	170	175	180	185	190	195	200
Expected:	5.81	4.37	3.20	2.57	2.09	1.81	1.54	1.31	1.10	0.79	0.72	0.91	1.07	1.32	1.68	2.05	2.43	2.80
Observed:	10.59	5.87	4.59	3.18	3.42	2.76	1.89	1.63	1.41	0.80	0.74	0.99	1.60	1.35	1.87	2.37	3.02	3.98

- 
- [1] R. Barate *et al.* [LEP Working Group for Higgs boson searches], Phys. Lett. B **565**, 61 (2003), [arXiv:hep-ex/0306033].
- [2] T. Aaltonen *et al.* (CDF Collaboration) Phys. Rev. Lett. **108**, 151803 (2012).
- [3] V. M. Abazov *et al.* (D0 Collaboration) Phys. Rev. Lett. **108**, 151804 (2012).
- [4] The LEP Electroweak Working Group, "Status of March 2012", <http://lepewwg.web.cern.ch/LEPEWWG/>.
- [5] CMS Collaboration, Phys. Lett. B **710**, 284 (2012); CMS Collaboration, arXiv:1202.4195 [hep-ex] (2012).
- [6] ATLAS Collaboration, Phys. Rev. Lett. **107**, 231801 (2011); ATLAS Collaboration, Phys. Lett. B **710**, 49 (2012).
- [7] V. M. Abazov *et al.* (D0 Collaboration), Nucl. Instrum. Methods Phys. Res. A **565**, 463 (2006);  
M. Abolins *et al.*, Nucl. Instrum. Methods Phys. Res. A **584**, 75 (2008);  
R. Angstadt *et al.*, Nucl. Instrum. Methods Phys. Res. A **622**, 298 (2010).
- [8] DØ Collaboration, DØ Note 6304-CONF (2012).
- [9] V. M. Abazov *et al.* (D0 Collaboration), Nucl. Instrum. Methods Phys. Res. A **620**, 490 (2010) [arXiv:1002.4224].
- [10] DØ Collaboration, DØ Note 6342-CONF (2012).
- [11] DØ Collaboration, DØ Note 6340-CONF (2012).
- [12] DØ Collaboration, DØ Note 6346-CONF (2012).
- [13] DØ Collaboration, DØ Note 6343-CONF (2012).
- [14] DØ Collaboration, DØ Note 6301-CONF (2012).
- [15] DØ Collaboration, DØ Note 6347-CONF (2012).
- [16] DØ Collaboration, DØ Note 6345-CONF (2012).
- [17] DØ Collaboration, DØ Note 6305-CONF (2012).
- [18] DØ Collaboration, DØ Note 6286-CONF (2012).
- [19] DØ Collaboration, Phys. Rev. Lett. **106** (2011) 171802 [arXiv:1101.6079v2 [hep-ph]].
- [20] All DØ conference notes are available from:  
<http://www-d0.fnal.gov/Run2Physics/WWW/results/higgs.htm>.
- [21] DØ Collaboration, DØ Note 6296-CONF (2012).
- [22] DØ Collaboration, DØ Note 6299-CONF (2012).
- [23] DØ Collaboration, DØ Note 6309-CONF (2012).
- [24] DØ Collaboration, DØ Note 6302-CONF (2012).
- [25] DØ Collaboration, DØ Note 6276-CONF (2012).
- [26] DØ Collaboration, DØ Note 6295-CONF (2012).
- [27] T. Sjöstrand, L. Lonnblad and S. Mrenna, arXiv:hep-ph/0108264 (2001).
- [28] M. L. Mangano, M. Moretti, F. Piccinini, R. Pittau and A. D. Polosa, JHEP **0307**, 001 (2003). [arXiv:hep-ph/0206293].
- [29] T. Gleisberg, *et al.*, JHEP **0902**, 007 (2009). [arXiv:hep-ph/0811.4622].
- [30] E. Boos, V. Bunichev, L. Dudko, V. Savrin, and A. Sherstnev, Phys. Atom. Nucl. **69**, 1317 (2006).
- [31] J. Campbell and R. K. Ellis, <http://mcfm.fnal.gov/>.  
J. M. Campbell, R. K. Ellis, Nucl. Phys. Proc. Suppl. **205-206**, 10 (2010). [arXiv:1007.3492 [hep-ph]].
- [32] U. Langenfeld, S. Moch and P. Uwer, Phys. Rev. D **80**, 054009 (2009).
- [33] N. Kidonakis, Phys. Rev. D **74**, 114012 (2006).
- [34] The CDF and DØ Collaborations and the TEVNPHWG Working Group, "Combined CDF and D0 Searches for Standard Model Higgs-Boson Production with up to 10 fb<sup>-1</sup> of Data", arXiv:1203.3774v1 [hep-ex] (2012);  
The CDF and DØ Collaborations and the TEVNPHWG Working Group, "Updated Combination of CDF and D0 Searches for Standard Model Higgs-Boson Production with up to 10 fb<sup>-1</sup> of Data", FERMILAB-CONF-12-318-E, CDF Note 10884, DØ Note 6348.
- [35] H. L. Lai *et al.*, Phys. Rev D **55**, 1280 (1997);  
P. M. Nadolsky *et al.*, Phys. Rev. D **78**, 013004 (2008).
- [36] G. Bozzi, S. Catani, D. de Florian, and M. Grazzini, Phys. Lett. B **564**, 65 (2003);  
G. Bozzi, S. Catani, D. de Florian, and M. Grazzini, Nucl. Phys. B **737**, 73 (2006).
- [37] C. Balazs, J. Huston, I. Puljak, Phys. Rev. D **63**, 014021 (2001).  
C. Balazs and C.-P. Yuan, Phys. Lett. B **478**, 192 (2000).  
Qing-Hong Cao and Chuan-Ren Chen, Phys. Rev. D **76**, 073006 (2007).
- [38] C. Anastasiou, R. Boughezal and F. Petriello, JHEP **0904**, 003 (2009).
- [39] D. de Florian and M. Grazzini, Phys. Lett. B **674**, 291 (2009).
- [40] M. Grazzini, private communication (2010).
- [41] The CDF and DØ Collaborations and the Tevatron Electroweak Working Group, arXiv:1007.3178 [hep-ex], arXiv:0903.2503 [hep-ex].
- [42] R. V. Harlander and W. B. Kilgore, Phys. Rev. Lett. **88**, 201801 (2002).
- [43] C. Anastasiou and K. Melnikov, Nucl. Phys. B **646**, 220 (2002).
- [44] V. Ravindran, J. Smith, and W. L. van Neerven, Nucl. Phys. B **665**, 325 (2003).
- [45] S. Actis, G. Passarino, C. Sturm, and S. Uccirati, Phys. Lett. B **670**, 12 (2008).
- [46] U. Aglietti, R. Bonciani, G. Degrossi, A. Vicini, arXiv:hep-ph/0610033v1 (2006).
- [47] S. Catani, D. de Florian, M. Grazzini and P. Nason, JHEP **0307**, 028 (2003) [arXiv:hep-ph/0306211].

- [48] A. D. Martin, W. J. Stirling, R. S. Thorne and G. Watt, *Eur. Phys. J. C* **63**, 189 (2009).
- [49] <http://www.hep.ucl.ac.uk/pdf4lhc/>;  
 S. Alekhin *et al.*, (PDF4LHC Working Group), [arXiv:1101.0536v1 [hep-ph]];  
 M. Botje *et al.*, (PDF4LHC Working Group), [arXiv:1101.0538v1 [hep-ph]].
- [50] I. W. Stewart, F. J. Tackmann, [arXiv:1107.2117 [hep-ph]].
- [51] C. Anastasiou, G. Dissertori, M. Grazzini, F. Stöckli and B. R. Webber, *JHEP* **0908**, 099 (2009). [arXiv:0905.3529 [hep-ph]].
- [52] J. M. Campbell, R. K. Ellis, C. Williams, *Phys. Rev.* **D81**, 074023 (2010). [arXiv:1001.4495 [hep-ph]].
- [53] J. Baglio and A. Djouadi, *JHEP* **1010**, 064 (2010) [arXiv:1003.4266v2 [hep-ph]].
- [54] The Fortran program can be found on Michael Spira's web page <http://people.web.psi.ch/~mspira/proglist.html>.
- [55] O. Brein, A. Djouadi, and R. Harlander, *Phys. Lett. B* **579**, 149 (2004).
- [56] M. L. Ciccolini, S. Dittmaier, and M. Kramer, *Phys. Rev. D* **68**, 073003 (2003).
- [57] P. Bolzoni, F. Maltoni, S.-O. Moch, and M. Zaro, *Phys. Rev. Lett.* **105**, 011801 (2010) [arXiv:1003.4451v2 [hep-ph]].
- [58] M. Ciccolini, A. Denner, and S. Dittmaier, *Phys. Rev. Lett.* **99**, 161803 (2007) [arXiv:0707.0381 [hep-ph]];  
 M. Ciccolini, A. Denner, and S. Dittmaier, *Phys. Rev. D* **77**, 013002 (2008) [arXiv:0710.4749 [hep-ph]].  
 We would like to thank the authors of the HAWK program for adapting it to the Tevatron.
- [59] A. Djouadi, J. Kalinowski and M. Spira, *Comput. Phys. Commun.* **108**, 56 (1998).
- [60] J. Baglio and A. Djouadi, arXiv:1012.0530 [hep-ph] (2010).
- [61] T. Junk, *Nucl. Instrum. Methods Phys. Res. A* **434**, 435 (1999); A.Read, CERN 2000-005 (30 May 2000).
- [62] T. Andeen *et al.*, Report No. FERMILAB-TM-2365 (2007).
- [63] W. Fisher, FERMILAB-TM-2386-E (2006).
- [64] O.J. Dunn, "Multiple Comparisons Among Means", *Journal of the American Statistical Association*, **56**, 52 (1961).

# Appendices

## Appendix A: Systematic Uncertainties

TABLE VII: Systematic uncertainties on the contributions for D0's  $ZH \rightarrow \ell^+ \ell^- b\bar{b}$  channels. Systematic uncertainties are listed by name; see the original references for a detailed explanation of their meaning and on how they are derived. Systematic uncertainties for  $ZH$  shown in this table are obtained for  $m_H = 125 \text{ GeV}/c^2$ . Uncertainties are relative, in percent, and are symmetric unless otherwise indicated. Shape uncertainties are labeled with an "(S)".

$ZH \rightarrow \ell\ell b\bar{b}$  Single Tag (ST) channel relative uncertainties (%) in the  $t\bar{t}$  depleted region

Contribution	$ZH$	Multijet	$Z+l.f.$	$Z+b\bar{b}$	$Z+c\bar{c}$	Dibosons	Top
Jet Energy Scale (S)	0.6	–	3.1	2.3	2.3	4.8	0.3
Jet Energy Resolution (S)	0.7	–	2.7	1.3	1.6	1.0	1.1
Jet ID (S)	0.6	–	1.5	0.0	0.5	0.7	0.7
Taggability (S)	2.0	–	1.9	1.7	1.7	1.8	2.2
$Z_{pT}$ Model (S)	–	–	1.6	1.7	1.5	–	–
HF Tagging Efficiency (S)	0.5	–	–	1.6	3.9	–	0.7
LF Tagging Efficiency (S)	–	–	68	–	–	2.9	–
$ee$ Multijet Shape (S)	–	45	–	–	–	–	–
Multijet Normalization	–	10	–	–	–	–	–
$Z$ +jets Jet Angles (S)	–	–	1.7	1.7	1.7	–	–
Alpgen MLM (S)	–	–	0.2	–	–	–	–
Alpgen Scale (S)	–	–	0.3	0.5	0.5	–	–
Underlying Event (S)	–	–	0.4	0.4	0.4	–	–
Trigger (S)	0.4-2	–	0.03-2	0.2-2	0.2-2	0.2-2	0.5-2
Cross Sections	6	–	–	20	20	7	10
Signal Branching Fraction	1-9	–	–	–	–	–	–
Normalization	5	–	4	4	4	6	5
PDFs	0.6	–	1.0	2.4	1.1	0.7	5.9

$ZH \rightarrow \ell\ell b\bar{b}$  Double Tag (DT) channel relative uncertainties (%) in the  $t\bar{t}$  depleted region

Contribution	$ZH$	Multijet	$Z+l.f.$	$Z+b\bar{b}$	$Z+c\bar{c}$	Dibosons	Top
Jet Energy Scale (S)	0.5	–	4.6	3.0	1.3	4.5	1.4
Jet Energy Resolution(S)	0.4	–	7.0	1.8	2.9	0.9	0.9
JET ID (S)	0.6	–	7.9	0.3	0.5	0.5	0.5
Taggability (S)	1.7	–	7.0	1.5	1.5	3.0	1.7
$Z_{pT}$ Model (S)	–	–	2.9	1.4	1.9	–	–
HF Tagging Efficiency (S)	4.4	–	–	5.0	5.6	–	3.8
LF Tagging Efficiency (S)	–	–	75	–	–	4.7	–
$ee$ Multijet Shape (S)	–	66	–	–	–	–	–
Multijet Normalization	–	10	–	–	–	–	–
$Z$ +jets Jet Angles (S)	–	–	1.9	3.5	3.8	–	–
Alpgen MLM (S)	–	–	0.2	–	–	–	–
Alpgen Scale (S)	–	–	0.4	0.5	0.5	–	–
Underlying Event(S)	–	–	0.5	0.4	0.4	–	–
Trigger (S)	0.4-2	–	0.6-6	0.3-2	0.3-3	0.4-2	0.6-5
Cross Sections	6	–	–	20	20	7	10
Signal Branching Fraction	1-9	–	–	–	–	–	–
Normalization	5	–	4	4	4	6	5
PDFs	0.6	–	1.0	2.4	1.1	0.7	5.9

$ZH \rightarrow \ell\ell b\bar{b}$  Single Tag (ST) channel relative uncertainties (%) in the  $t\bar{t}$  enriched region

Contribution	$ZH$	Multijet	$Z+l.f.$	$Z+b\bar{b}$	$Z+c\bar{c}$	Dibosons	Top
Jet Energy Scale (S)	7.5	–	4.6	1.7	3.9	11	2.5
Jet Energy Resolution (S)	0.2	–	4.5	0.7	3.1	3.9	0.7
Jet ID (S)	1.2	–	2.1	1.0	1.2	0.9	0.7
Taggability (S)	2.1	–	7.3	2.7	3.0	2.0	3.2
$Z_{pT}$ Model (S)	–	–	3.3	1.5	1.4	–	–
HF Tagging Efficiency (S)	0.5	–	–	1.3	4.8	–	0.8
LF Tagging Efficiency (S)	–	–	73	–	–	4.1	–
$ee$ Multijet Shape (S)	–	59	–	–	–	–	–
Multijet Normalization	–	10	–	–	–	–	–
$Z$ +jets Jet Angles (S)	–	–	1.7	2.3	2.7	–	–
AlpGen MLM (S)	–	–	0.4	–	–	–	–
AlpGen Scale (S)	–	–	0.7	0.7	0.7	–	–
Underlying Event (S)	–	–	0.9	1.1	1.1	–	–
Trigger (S)	1-4	–	1-4	0.7-4	0.7-4	1-8	1-8
Cross Sections	6	–	–	20	20	7	10
Signal Branching Fraction	1-9	–	–	–	–	–	–
Normalization	5	–	4	4	4	6	5
PDFs	0.6	–	1.0	2.4	1.1	0.7	5.9

 $ZH \rightarrow \ell\ell b\bar{b}$  Double Tag (DT) channel relative uncertainties (%) in the  $t\bar{t}$  enriched region

Contribution	$ZH$	Multijet	$Z+l.f.$	$Z+b\bar{b}$	$Z+c\bar{c}$	Dibosons	Top
Jet Energy Scale (S)	6.6	–	0.8	1.6	2.2	5.9	1.5
Jet Energy Resolution(S)	1.4	–	267	1.4	2.1	4.0	0.4
JET ID (S)	0.9	–	0.6	0.5	3.6	2.8	0.6
Taggability (S)	2.0	–	0.9	1.6	1.9	3.1	2.1
$Z_{pT}$ Model (S)	–	–	1.8	1.4	1.5	–	–
HF Tagging Efficiency (S)	4.0	–	–	5.1	6.6	–	4.2
LF Tagging Efficiency (S)	–	–	72	–	–	–	–
$ee$ Multijet Shape (S)	–	91	–	–	–	–	–
Multijet Normalization	–	10	–	–	–	–	–
$Z$ +jets Jet Angles (S)	–	–	1.4	3.7	2.3	–	–
AlpGen MLM (S)	–	–	0.5	–	–	–	–
AlpGen Scale (S)	–	–	0.8	0.5	0.4	–	–
Underlying Event(S)	–	–	0.9	0.7	0.5	–	–
Trigger (S)	1-3	–	1-3	0.6-3	0.7-4	0.7-4	1-3
Cross Sections	6	–	–	20	20	7	10
Signal Branching Fraction	1-9	–	–	–	–	–	–
Normalization	5	–	4	4	4	6	5
PDFs	0.6	–	1.0	2.4	1.1	0.7	5.9

TABLE VIII: Systematic uncertainty ranges on the signal and background contributions and the error on the total background for D0's  $ZH \rightarrow \nu\nu b\bar{b}$  medium-tag and tight-tag channels. Systematic uncertainties are listed by name, see the original references for a detailed explanation of their meaning and on how they are derived. Systematic uncertainties for  $VH$  ( $WH+ZH$ ) shown in this table are obtained for  $m_H = 115 \text{ GeV}/c^2$ . Uncertainties are relative, in percent, and are symmetric unless otherwise indicated. Shape uncertainties are labeled with an “(S)”, and “SH” represents shape only uncertainty.

$ZH \rightarrow \nu\nu b\bar{b}$  medium-tag channel relative uncertainties (%)

Contribution	Top	$V + b\bar{b}/c\bar{c}$	$V+l.f.$	Dibosons	Total Bkgd	$VH$
Jet ID/Reco Eff (S)	2.0	2.0	2.0	2.0	1.9	2.0
Jet Energy Scale (S)	1.3	1.5	2.8	1.5	1.9	0.3
Jet Resolution (S)	0.5	0.4	0.5	0.8	0.5	0.9
Vertex Conf. / Taggability (S)	3.4	2.2	2.0	2.3	2.2	2.1
b Tagging (S)	1.5	2.6	8.0	3.6	3.7	0.6
Lepton Identification	1.5	0.9	0.8	0.9	0.9	0.9
Trigger	2.0	2.0	2.0	2.0	1.9	2.0
Heavy Flavor Fractions	–	20.0	–	–	8.4	–
Cross Sections	10.0	10.2	10.2	7.0	9.8	7.0
Signal Branching Fraction	–	–	–	–	–	1-9
Luminosity	6.1	6.1	6.1	6.1	5.8	6.1
Multijet Normalization	–	–	–	–	1.1	–
ALPGEN MLM (S)	–	–	SH	–	–	–
ALPGEN Scale (S)	–	SH	SH	–	–	–
Underlying Event (S)	–	SH	SH	–	–	–
PDF, reweighting (S)	SH	SH	SH	SH	SH	SH
Total uncertainty	12.8	23.8	15.1	10.8	14.2	10.0

$ZH \rightarrow \nu\nu b\bar{b}$  tight-tag channel relative uncertainties (%)

Contribution	Top	$V + b\bar{b}/c\bar{c}$	$V+l.f.$	Dibosons	Total Bkgd	$VH$
Jet ID/Reco Eff (S)	2.0	2.0	2.0	2.0	2.0	2.0
Jet Energy Scale (S)	1.0	1.6	3.9	1.6	1.6	0.5
Jet Resolution (S)	0.7	0.6	2.6	1.4	0.8	1.3
Vertex Conf. / Taggability (S)	3.0	1.9	2.4	2.0	2.3	1.9
b Tagging (S)	8.9	7.3	12.5	6.4	7.4	7.8
Lepton Identification	1.9	0.8	0.3	0.7	1.1	0.8
Trigger	2.0	2.0	2.0	2.0	2.0	2.0
Heavy Flavor Fractions	–	20.0	–	–	11.0	–
Cross Sections	10.0	10.2	10.2	7.0	10.0	7.0
Signal Branching Fraction	–	–	–	–	–	1-9
Luminosity	6.1	6.1	6.1	6.1	6.1	6.1
Multijet Normalization	–	–	–	–	0.2	–
ALPGEN MLM (S)	–	–	SH	–	–	–
ALPGEN Scale (S)	–	SH	SH	–	–	–
Underlying Event (S)	–	SH	SH	–	–	–
PDF, reweighting (S)	SH	SH	SH	SH	SH	SH
Total uncertainty	15.5	24.7	18.3	12.0	16.8	12.7

TABLE IX: Systematic uncertainties on the signal and background contributions for D0's  $WH \rightarrow \ell\nu b\bar{b}$  single and double tag channels. Systematic uncertainties are listed by name, see the original references for a detailed explanation of their meaning and on how they are derived. Systematic uncertainties for  $WH$  shown in this table are obtained for  $m_H = 115 \text{ GeV}/c^2$ . Uncertainties are relative, in percent, and are symmetric unless otherwise indicated. Shape uncertainties are labeled with an “(S)”, and “SH” represents shape only uncertainty.

$WH \rightarrow \ell\nu b\bar{b}$  Single Tag (TST) channels relative uncertainties (%)

Contribution	Dibosons	$W + b\bar{b}/c\bar{c}$	$W+l.f.$	$t\bar{t}$	single top	Multijet	$WH$
Luminosity	6.1	6.1	6.1	6.1	6.1	–	6.1
Electron ID/Trigger eff. (S)	1–5	2–4	2–4	1–2	1–2	–	2–3
Muon Trigger eff. (S)	1	1	1	1	1	–	1
Muon ID/Reco eff./resol.	4.1	4.1	4.1	4.1	4.1	–	4.1
Jet ID/Reco eff.	2	2	2	2	2	–	2
Jet Resolution (S)	1–2	2–4	2–3	2–5	1–2	–	2
Jet Energy Scale (S)	4–7	1–5	2–5	2–7	1–2	–	2–6
Vertex Conf. Jet (S)	4–6	3–4	2–3	6–10	2–4	–	3–7
$b$ -tag/taggability (S)	1–3	1–4	7–10	1–6	1–2	–	2–9
Heavy-Flavor K-factor	–	20	–	–	–	–	–
Inst.-WH $e\nu b\bar{b}$ (S)	1–2	2–4	1–3	1–2	1–3	15	1–2
Inst.-WH $\mu\nu b\bar{b}$	–	2.4	2.4	–	–	20	–
Cross Section	6	9	6	7	7	–	6.1
Signal Branching Fraction	–	–	–	–	–	–	1-9
ALPGEN MLM pos/neg(S)	–	–	SH	–	–	–	–
ALPGEN Scale (S)	–	SH	SH	–	–	–	–
Underlying Event (S)	–	SH	SH	–	–	–	–
PDF, reweighting	2	2	2	2	2	–	2

$WH \rightarrow \ell\nu b\bar{b}$  Loose Double Tag (LDT) channels relative uncertainties (%)

Contribution	Dibosons	$W + b\bar{b}/c\bar{c}$	$W+l.f.$	$t\bar{t}$	single top	Multijet	$WH$
Luminosity	6.1	6.1	6.1	6.1	6.1	–	6.1
Electron ID/Trigger eff. (S)	2–5	2–3	2–3	1–2	1–2	–	1–2
Muon Trigger eff. (S)	1	1	1	1	1	–	1
Muon ID/Reco eff./resol.	4.1	4.1	4.1	4.1	4.1	–	4.1
Jet ID/Reco eff.	2	2	2	2	2	–	2
Jet Resolution (S)	1–7	2–7	2–3	2–7	2–4	–	1–5
Jet Energy Scale (S)	2–11	2–5	2–7	2–7	2–5	–	2–8
Vertex Conf. Jet (S)	2–11	2–12	2–3	4–15	2–3	–	3–7
$b$ -tag/taggability (S)	2–15	2–6	6–10	2–5	2–3	–	1–5
Heavy-Flavor K-factor	–	20	–	–	–	–	–
Inst.-WH $e\nu b\bar{b}$ (S)	1–2	2–4	1–3	1–2	1–3	15	1–2
Inst.-WH $\mu\nu b\bar{b}$	–	2.4	2.4	–	–	20	–
Cross Section	6	9	6	7	7	–	6.1
Signal Branching Fraction	–	–	–	–	–	–	1-9
ALPGEN MLM pos/neg(S)	–	–	SH	–	–	–	–
ALPGEN Scale (S)	–	SH	SH	–	–	–	–
Underlying Event (S)	–	SH	SH	–	–	–	–
PDF, reweighting	2	2	2	2	2	–	2

$WH \rightarrow \ell\nu b\bar{b}$  Medium Double Tag (MDT) channels relative uncertainties (%)

Contribution	Dibosons	$W + b\bar{b}/c\bar{c}$	$W+l.f.$	$t\bar{t}$	single top	Multijet	$WH$
Luminosity	6.1	6.1	6.1	6.1	6.1	–	6.1
Electron ID/Trigger eff. (S)	2–5	2–3	2–3	1–2	1–2	–	1–2
Muon Trigger eff. (S)	2–5	1–3	1–3	1–5	2–3	–	1–3
Muon ID/Reco eff./resol.	4.1	4.1	4.1	4.1	4.1	–	4.1
Jet ID/Reco eff.	2	2	2	2	2	–	2
Jet Resolution (S)	2–15	2–10	5–20	1–3	1–3	–	1–10
Jet Energy Scale (S)	2–10	2–20	1–8	1–5	1–5	–	2–10
Vertex Conf. Jet (S)	1–5	2–3	2–7	5–7	2–3	–	2–4
$b$ -tag/taggability (S)	3–15	4–15	10–15	4–10	3–9	–	2–5
Heavy-Flavor K-factor	–	20	–	–	–	–	–
Inst.-WH $e\nu b\bar{b}$ (S)	1–2	2–4	1–3	1–2	1–3	15	1–2
Inst.-WH $\mu\nu b\bar{b}$	–	2.4	2.4	–	–	20	–
Cross Section	6	9	6	7	7	–	6.1
Signal Branching Fraction	–	–	–	–	–	–	1–9
ALPGEN MLM pos/neg(S)	–	–	SH	–	–	–	–
ALPGEN Scale (S)	–	SH	SH	–	–	–	–
Underlying Event (S)	–	SH	SH	–	–	–	–
PDF, reweighting	2	2	2	2	2	–	2

 $WH \rightarrow \ell\nu b\bar{b}$  Tight Double Tag (TDT) channels relative uncertainties (%)

Contribution	Dibosons	$W + b\bar{b}/c\bar{c}$	$W+l.f.$	$t\bar{t}$	single top	Multijet	$WH$
Luminosity	6.1	6.1	6.1	6.1	6.1	–	6.1
Electron ID/Trigger eff. (S)	2–5	2–3	2–3	1–2	1–2	–	1–2
Muon Trigger eff. (S)	1	1	1	1	1	–	1
Muon ID/Reco eff./resol.	4.1	4.1	4.1	4.1	4.1	–	4.1
Jet ID/Reco eff.	2	2	2	2	2	–	2
Jet Resolution (S)	2–5	4–7	2–6	1–4	2–6	–	2–9
Jet Energy Scale (S)	2–15	2–8	1–8	2–7	1–4	–	1–9
Vertex Conf. Jet (S)	2–3	2–4	2–5	5–6	2–3	–	2–4
$b$ -tag/taggability (S)	3–15	5–10	5–15	6–10	5–10	–	5–12
Heavy-Flavor K-factor	–	20	–	–	–	–	–
Inst.-WH $e\nu b\bar{b}$ (S)	1–2	2–4	1–3	1–2	1–3	15	1–2
Inst.-WH $\mu\nu b\bar{b}$	–	2.4	2.4	–	–	20	–
Cross Section	6	9	6	7	7	–	6.1
Signal Branching Fraction	–	–	–	–	–	–	1–9
ALPGEN MLM pos/neg(S)	–	–	SH	–	–	–	–
ALPGEN Scale (S)	–	SH	SH	–	–	–	–
Underlying Event (S)	–	SH	SH	–	–	–	–
PDF, reweighting	2	2	2	2	2	–	2



TABLE X: Systematic uncertainties on the signal and background contributions for D0's  $H \rightarrow W^+W^- \rightarrow \ell^\pm \ell^\mp$  channels. Systematic uncertainties are listed by name; see the original references for a detailed explanation of their meaning and on how they are derived. Shape uncertainties are labeled with the “s” designation. Systematic uncertainties given in this table are obtained for the  $m_H = 165 \text{ GeV}/c^2$  Higgs selection. Cross section uncertainties on the  $gg \rightarrow H$  signal depend on the jet multiplicity, as described in the main text. Uncertainties are relative, in percent, and are symmetric unless otherwise indicated.

$H \rightarrow W^+W^- \rightarrow \ell^\pm \ell^\mp$  channels relative uncertainties (%)

Contribution	Dibosons	$Z/\gamma^* \rightarrow \ell\ell$	$W+\text{jet}/\gamma$	$t\bar{t}$	Multijet	$gg \rightarrow H$	$qq \rightarrow qqH$	$VH$
Luminosity/Normalization	4	–	4	4	4	4	4	4
Cross Section (Scale/PDF)	5-7	–	–	7	–	13-33/8-30	5	6
$Z/\gamma^* \rightarrow \ell\ell$ n-jet norm	–	2-15	–	–	–	–	–	–
$Z/\gamma^* \rightarrow \ell\ell$ MET model	–	5-19	–	–	–	–	–	–
$W+\text{jet}/\gamma$ norm	–	–	6-30	–	–	–	–	–
$W+\text{jet}/\gamma$ ISR/FSR model (s)	–	–	2-20	–	–	–	–	–
Vertex Confirmation (s)	1-5	1-5	1-5	5-6	–	1-5	1-5	1-5
Jet identification (s)	1	1	1	1	–	1	1	1
Jet Energy Scale (s)	1-5	1-5	1-5	1-4	–	1-5	1-5	1-4
Jet Energy Resolution(s)	1-4	1-4	1-4	1-4	–	1-3	1-4	1-3
B-tagging (s)	–	–	–	1-5	–	–	–	–

TABLE XI: Systematic uncertainties on the signal and background contributions for D0's  $H \rightarrow W^+W^- \rightarrow \mu\nu\tau_{\text{had}}\nu$  channel. Systematic uncertainties are listed by name; see the original references for a detailed explanation of their meaning and on how they are derived. Shape uncertainties are labeled with the shape designation (S). Systematic uncertainties shown in this table are obtained for the  $m_H = 165 \text{ GeV}/c^2$  Higgs selection. Uncertainties are relative, in percent, and are symmetric unless otherwise indicated.

$H \rightarrow W^+W^- \rightarrow \mu\nu\tau_{\text{had}}\nu$  channel relative uncertainties (%)

Contribution	Diboson	$Z/\gamma^* \rightarrow \ell\ell$	$W+\text{jets}$	$t\bar{t}$	Multijet	$gg \rightarrow H$	$qq \rightarrow qqH$	$VH$
Luminosity ( $\sigma_{\text{inel}}(pp)$ )	4.6	4.6	–	4.6	–	4.6	4.6	4.6
Luminosity Monitor	4.1	4.1	–	4.1	–	4.1	4.1	4.1
Trigger	5.0	5.0	–	5.0	–	5.0	5.0	5.0
Lepton ID	3.7	3.7	–	3.7	–	3.7	3.7	3.7
EM veto	5.0	–	–	5.0	–	5.0	5.0	5.0
Tau Energy Scale (S)	1.0	1.1	–	<1	–	<1	<1	<1
Jet Energy Scale (S)	8.0	<1	–	1.8	–	2.5	2.5	2.5
Jet identification (S)	<1	<1	–	7.5	–	5.0	5.0	5.0
Multijet (S)	–	–	–	–	20-50	–	–	–
Cross Section (scale/PDF)	7.0	4.0	–	10	–	7/8	4.9	6.1
Signal Branching Fraction	–	–	–	–	–	0-7.3	0-7.3	0-7.3
Modeling	1.0	–	10	–	–	3.0	3.0	3.0

TABLE XII: Systematic uncertainties on the signal and background contributions for D0's  $VH \rightarrow e^\pm \nu_e \mu^\pm \nu_\mu$  ( $V = W, Z$ ) channels. Systematic uncertainties are listed by name; see the original references for a detailed explanation of their meaning and on how they are derived. Shape uncertainties are labeled with the “shape” designation. Systematic uncertainties shown in this table are obtained for the  $m_H = 165 \text{ GeV}/c^2$  Higgs selection. Uncertainties are relative, in percent, and are symmetric unless otherwise indicated.

$VH \rightarrow e^\pm \nu_e \mu^\pm \nu_\mu$ like charge electron muon pair channel relative uncertainties (%)						
Contribution	VH	$Z + jet/\gamma$	$W + jet/\gamma$	$t\bar{t}$	Diboson	Multijet
Cross section	6.2	–	–	6	7	–
Luminosity/Normalization	4	–	4	4	4	–
Multijet	–	–	–	–	–	30
Trigger	2	2	2	2	2	2
Charge flip	–	50	–	50	50	–
W+jets/ $\gamma$	–	–	10	–	–	–
$W - p_T$ model	–	–	shape	–	–	–
$Z - p_T$ model	–	shape	–	–	–	–
W+jets/ $\gamma$ ISR/FSR model	–	–	shape	–	–	–

TABLE XIII: Systematic uncertainties on the signal and background contributions for D0's  $VH \rightarrow VWW \rightarrow ee\mu, \mu\mu e$  channels. Systematic uncertainties are listed by name; see the original references for a detailed explanation of their meaning and on how they are derived. Shape uncertainties are labeled with the “s” designation. Systematic uncertainties given in this table are obtained for the  $m_H = 145 \text{ GeV}$  Higgs selection. Uncertainties are relative, in percent, and are symmetric unless otherwise indicated. Jet shape uncertainties are applied to the  $\mu\mu e$  channel only.

$VH \rightarrow VWW \rightarrow$ Trilepton channels relative uncertainties (%)								
Contribution	Dibosons	$Z/\gamma^* \rightarrow \ell\ell$	$W+jet/\gamma$	$t\bar{t}$	$Z\gamma$	$VH$	$gg \rightarrow H$	$qq \rightarrow qqH$
Luminosity	6.1	6.1	6.1	6.1	–	6.1	6.1	6.1
Cross Section (Scale/PDF)	6	6	6	7	–	6.2	7	4.9
PDF	2.5	2.5	2.5	2.5	–	2.5	2.5	2.5
Electron Identification	2.5	2.5	2.5	2.5	–	2.5	2.5	2.5
Muon Identification	4	4	4	4	–	4	4	4
Trigger	3.5	3.5	3.5	3.5	–	3.5	3.5	3.5
$Z\gamma$	–	–	–	–	9.5	–	–	–
$V + jets$ lepton fake rate	–	30	30	–	–	–	–	–
$Z-p_T$ reweighting (s)	–	$\pm 1\sigma$	–	–	–	–	–	–
Electron smearing (s)	$\pm 1\sigma$	$\pm 1\sigma$	$\pm 1\sigma$	$\pm 1\sigma$	–	$\pm 1\sigma$	$\pm 1\sigma$	$\pm 1\sigma$
Muon smearing (s)	$\pm 1\sigma$	$\pm 1\sigma$	$\pm 1\sigma$	$\pm 1\sigma$	–	$\pm 1\sigma$	$\pm 1\sigma$	$\pm 1\sigma$
Jet Shape systematics below applied to $\mu\mu e$ channel only								
Jet Energy Scale (s)	$\pm 1\sigma$	$\pm 1\sigma$	$\pm 1\sigma$	$\pm 1\sigma$	–	$\pm 1\sigma$	$\pm 1\sigma$	$\pm 1\sigma$
Jet Energy Resolution (s)	$\pm 1\sigma$	$\pm 1\sigma$	$\pm 1\sigma$	$\pm 1\sigma$	–	$\pm 1\sigma$	$\pm 1\sigma$	$\pm 1\sigma$
Jet Identification (s)	$-1\sigma$	$-1\sigma$	$-1\sigma$	$-1\sigma$	–	$-1\sigma$	$-1\sigma$	$-1\sigma$
Vertex Confirmation (s)	$-1\sigma$	$-1\sigma$	$-1\sigma$	$-1\sigma$	–	$-1\sigma$	$-1\sigma$	$-1\sigma$

TABLE XIV: Systematic uncertainties on the signal and background contributions for D0's  $\tau\tau\mu + X$  channel. Systematic uncertainties are listed by name; see the original references for a detailed explanation of their meaning and on how they are derived. Shape uncertainties are labeled with the “s” designation. Cross section uncertainties on the  $gg \rightarrow H$  signal depend on the jet multiplicity, as described in the main text. Uncertainties are relative, in percent, and are symmetric unless otherwise indicated.

$\tau\tau\mu + X$  channels relative uncertainties (%)

Contribution	Dibosons	$Z/\gamma^*$	$t\bar{t}$	Instrumental	$gg \rightarrow H$	$qq \rightarrow qqH$	$VH$
Luminosity/Normalization	6	6	6	24	6	6	6
Trigger	3	3	3	–	3	3	3
Cross Section (Scale/PDF)	7	6	10	–	13-33/7.6-30	4.9	6.2
PDF	2.5	2.5	2.5	–	2.5	2.5	2.5
Tau Id per $\tau$ (Type 1/2/3)	7/3.5/5	7/3.5/5	7/3.5/5	–	7/3.5/5	7/3.5/5	7/3.5/5
Tau Energy Scale	1	1	1	–	1	1	1
Tau Track Match per $\tau$	1.4	1.4	1.4	–	1.4	1.4	1.4
Muon Identification	2.9	2.9	2.9	–	2.9	2.9	2.9

TABLE XV: Systematic uncertainties on the signal and background contributions for the  $VH \rightarrow VWW^* \rightarrow \ell\nu jjjj$  analysis. Systematic uncertainties are listed by name; see the original references for a detailed explanation of their meaning and on how they are derived. Signal uncertainties are shown for the total signal contribution at  $m_H = 125 \text{ GeV}/c^2$  for all channels. Those affecting the shape of the RF discriminant are indicated with “Y.” Uncertainties are listed as relative changes in normalization, in percent, except for those also marked by “S,” where the overall normalization is constant, and the value given denotes the maximum percentage change from nominal in any region of the distribution.

D0:  $VH \rightarrow VWW^* \rightarrow \ell\nu jjjj$  Run II Zero Tag channel relative uncertainties (%)

Contribution	Dibosons	$W + b\bar{b}/c\bar{c}$	$W+l.f.$	Top quark	Multijet	Signal
Luminosity	6.1	6.1	6.1	6.1	–	6.1
Electron ID/Trigger eff. (S)	3	3	3	3	–	3
Muon Trigger eff. (S)	1	1	1	1	–	1
Muon ID/Reco eff./resol.	3	3	3	3	–	3
Jet ID/Reco eff.	2	2	2	2	–	2
Jet Resolution (S)	1–2	2–4	2–3	2–5	–	2
Jet Energy Scale (S)	5–10	1–5	2–7	2–7	–	2–6
Vertex Conf. Jet (S)	3–4	1–2	1–2	3–4	–	3–7
$b$ -tag/taggability (S)	4–5	1–3	1–3	5–10	–	4–10
Heavy-Flavor K-factor	–	20	–	–	–	–
Cross Section	6	9	6	7	–	6.1
Signal Branching Fraction	–	–	–	–	–	1–9
ALPGEN MLM pos/neg(S)	–	SH	–	–	–	–
ALPGEN Scale (S)	–	SH	SH	–	–	–
Underlying Event (S)	–	SH	–	–	–	–
PDF, reweighting	2	2	2	2	–	2

D0:  $VH \rightarrow VWW^* \rightarrow \ell\nu jjjj$  Run II Loose Single Tag channel relative uncertainties (%)

Contribution	Dibosons	$W + b\bar{b}/c\bar{c}$	$W+l.f.$	Top quark	Multijet	Signal
Luminosity	6.1	6.1	6.1	6.1	–	6.1
Electron ID/Trigger eff. (S)	3	3	3	3	–	3
Muon Trigger eff. (S)	1	1	1	1	–	1
Muon ID/Reco eff./resol.	3	3	3	3	–	3
Jet ID/Reco eff.	2	2	2	2	–	2
Jet Resolution (S)	1–2	2–4	2–3	2–5	–	2
Jet Energy Scale (S)	5–10	1–5	2–7	2–7	–	2–6
Vertex Conf. Jet (S)	3–4	1–2	1–2	3–4	–	3–5
$b$ -tag/taggability (S)	2–8	1–3	1–2	5–10	–	4–10
Heavy-Flavor K-factor	–	20	–	–	–	–
Cross Section	6	9	6	7	–	6.1
Signal Branching Fraction	–	–	–	–	–	1–9
ALPGEN MLM pos/neg(S)	–	SH	–	–	–	–
ALPGEN Scale (S)	–	SH	SH	–	–	–
Underlying Event (S)	–	SH	–	–	–	–
PDF, reweighting	2	2	2	2	–	2

TABLE XVI: Systematic uncertainties on the signal and background contributions for D0's  $H \rightarrow WW^* \rightarrow \ell\nu jj$  electron and muon channels. Systematic uncertainties are listed by name; see the original references for a detailed explanation of their meaning and on how they are derived. Signal uncertainties are shown for  $m_H = 160 \text{ GeV}/c^2$  for all channels except for  $WH$ , shown for  $m_H = 115 \text{ GeV}/c^2$ . Those affecting the shape of the RF discriminant are indicated with "Y." Uncertainties are listed as relative changes in normalization, in percent, except for those also marked by "S," where the overall normalization is constant, and the value given denotes the maximum percentage change from nominal in any region of the distribution.

$H \rightarrow WW^* \rightarrow \ell\nu jj$ Run II channel relative uncertainties (%)								
Contribution	Shape	$W$ +jets	$Z$ +jets	Top	Diboson	$gg \rightarrow H$	$qq \rightarrow qqH$	$WH$
Jet energy scale	Y	$(+6.7)_{-5.4}^S$	< 0.1	$\pm 0.7$	$\pm 3.3$	$(+5.7)_{-4.0}$	$\pm 1.5$	$(+2.7)_{-2.3}$
Jet identification	Y	$\pm 6.6^S$	< 0.1	$\pm 0.5$	$\pm 3.8$	$\pm 1.0$	$\pm 1.1$	$\pm 1.0$
Jet resolution	Y	$(+6.6)_{-4.1}^S$	< 0.1	$\pm 0.5$	$(+1.0)_{-0.5}$	$(+3.0)_{-0.5}$	$\pm 0.8$	$\pm 1.0$
Association of jets with PV	Y	$\pm 3.2^S$	$\pm 1.3^S$	$\pm 1.2$	$\pm 3.2$	$\pm 2.9$	$\pm 2.4$	$(+0.9)_{-0.2}$
Luminosity	N	n/a	n/a	$\pm 6.1$	$\pm 6.1$	$\pm 6.1$	$\pm 6.1$	$\pm 6.1$
Muon trigger	Y	$\pm 0.4^S$	< 0.1	< 0.1	< 0.1	< 0.1	< 0.1	< 0.1
Electron identification	N	$\pm 4.0$	$\pm 4.0$	$\pm 4.0$	$\pm 4.0$	$\pm 4.0$	$\pm 4.0$	$\pm 4.0$
Muon identification	N	$\pm 4.0$	$\pm 4.0$	$\pm 4.0$	$\pm 4.0$	$\pm 4.0$	$\pm 4.0$	$\pm 4.0$
ALPGEN tuning	Y	$\pm 1.1^S$	$\pm 0.3^S$	n/a	n/a	n/a	n/a	n/a
Cross Section	N	$\pm 6$	$\pm 6$	$\pm 10$	$\pm 7$	$\pm 10$	$\pm 10$	$\pm 6$
Heavy-flavor fraction	Y	$\pm 20$	$\pm 20$	n/a	n/a	n/a	n/a	n/a
Signal Branching Fraction	N	n/a	n/a	n/a	n/a	0-7.3	0-7.3	0-7.3
PDF	Y	$\pm 2.0^S$	$\pm 0.7^S$	< 0.1 <sup>S</sup>	< 0.1 <sup>S</sup>	< 0.1 <sup>S</sup>	< 0.1 <sup>S</sup>	< 0.1 <sup>S</sup>
			Electron channel			Muon channel		
Multijet Background	Y		$\pm 6.5$			$\pm 26$		

TABLE XVII: Systematic uncertainties on the signal and background contributions for D0's  $H \rightarrow \gamma\gamma$  channel. Systematic uncertainties for the Higgs signal shown in this table are obtained for  $m_H = 125 \text{ GeV}/c^2$ . Systematic uncertainties are listed by name; see the original references for a detailed explanation of their meaning and on how they are derived. Uncertainties are relative, in percent, and are symmetric unless otherwise indicated.

$H \rightarrow \gamma\gamma$ channel relative uncertainties (%)		
Contribution	Background	Signal
Luminosity	6	6
Acceptance	-	2
electron ID efficiency	2	-
electron track-match inefficiency	10	-
Photon ID efficiency	3	3
Cross Section	4	10
Background subtraction	15	-

## Appendix B: Comparison With Previous Results

Here we document a comparison of these results with those presented in Ref. [8]. In Fig. 15, we show comparisons of the expected and observed limits. The expected limits have improved by approximately 10%. There observed limits have not changed significantly, and exhibit fewer fluctuations between adjacent assumed values of  $m_H$ . Figure 16 compares the  $\log_{10}(s/b)$  distributions of the two results for Higgs boson masses of 115 GeV and 125 GeV. In this result, the distribution ranges to larger values of  $\log_{10}(s/b)$  than in the previous combination, indicating an increase in sensitivity. Figure 17 shows the corresponding background subtracted distributions. In Fig. 18, we compare the cumulative signal distributions. For  $m_H = 125$  GeV, the highest  $s/b$  bins contain an excess of signal like events in the current result that is more significant than the excess exhibited in Ref. [8]. Figures 19-21 and 22-24 show the same distributions for the combined  $WH/ZH, H \rightarrow b\bar{b}$  and the combined  $WH/ZH/H, H \rightarrow W^+W^-$  analyses respectively.

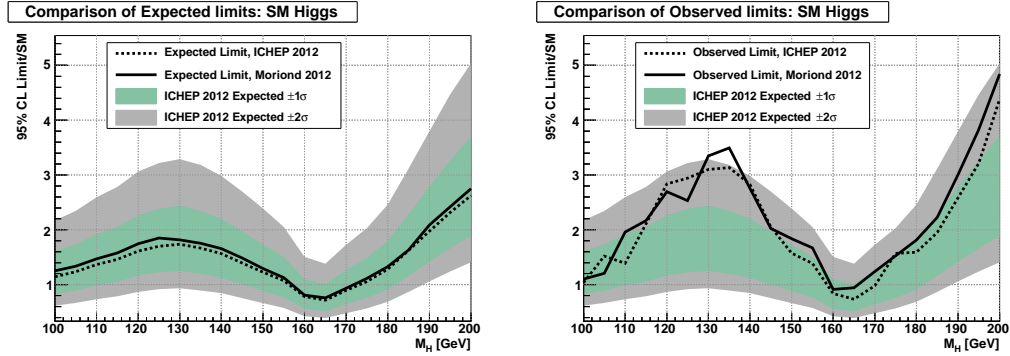


FIG. 15: Comparison of expected (median), and observed 95% C.L. cross section upper limit ratios for this result (right) and the result from Ref. [8] (left) over the  $100 \leq m_H \leq 200$  GeV mass range. The green and grey bands correspond to the regions enclosing 1 and 2 standard deviation fluctuations of the background, respectively.

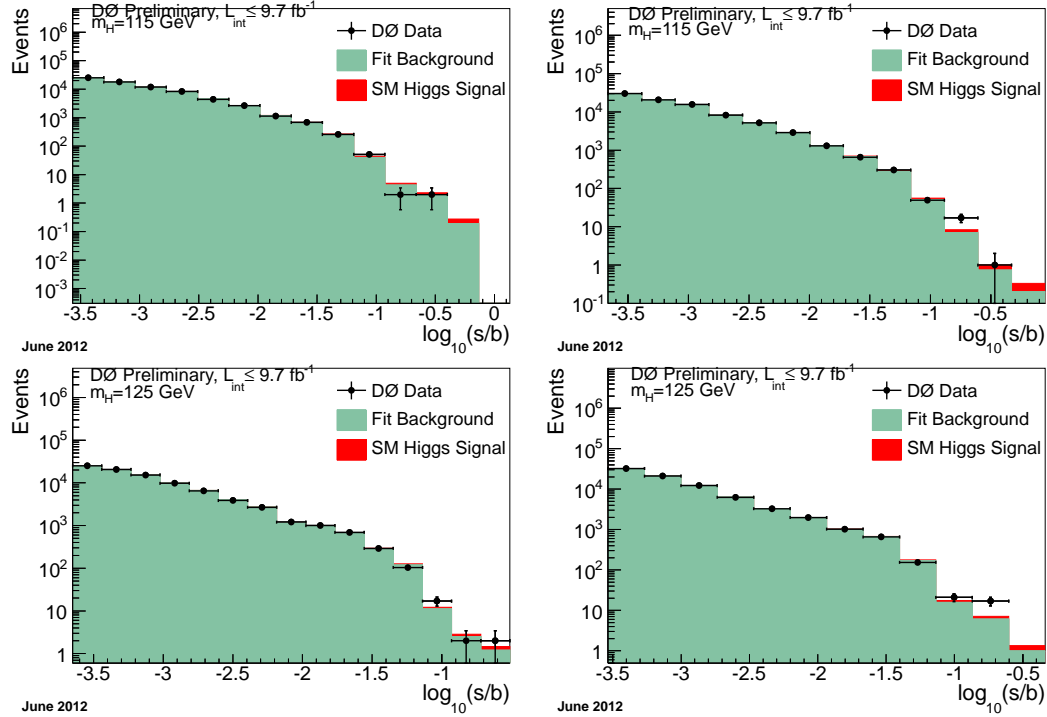


FIG. 16: Distributions of  $\log_{10}(s/b)$  from this result (right) and the result in Ref. [8] (left) for assumed Higgs boson masses of 115 GeV and 125 GeV. The data are shown with points and the expected signal is stacked on top of the sum of backgrounds. Only statistical uncertainties on the data points are shown.

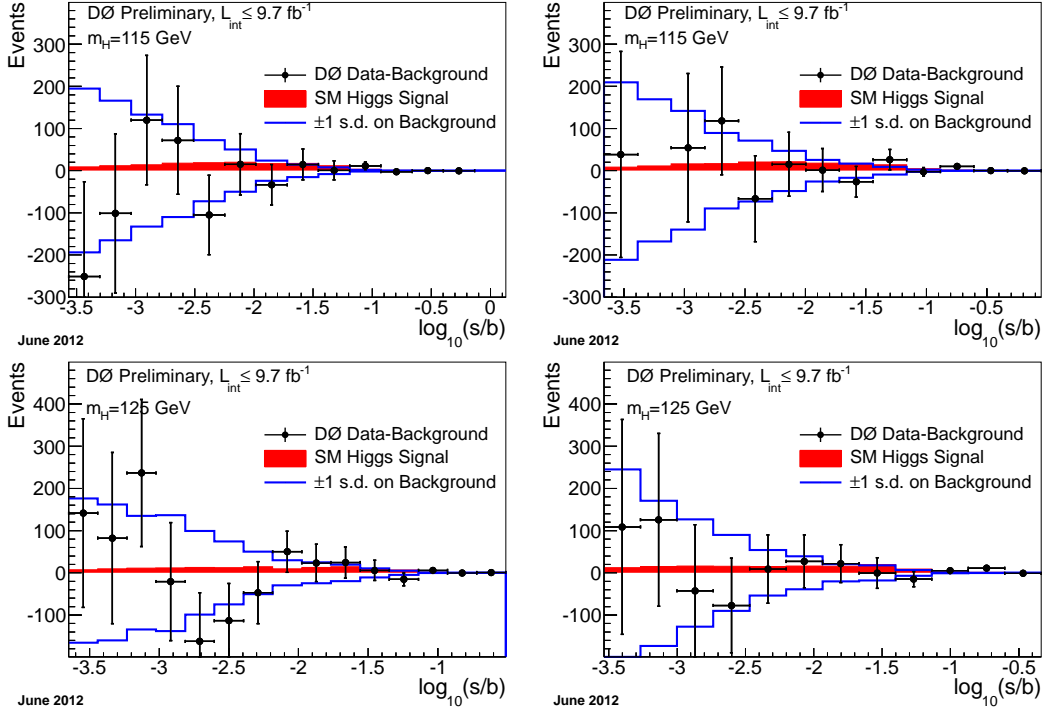


FIG. 17: Background-subtracted data distributions of  $\log_{10}(s/b)$  for this result (right) and the result from Ref. [8] (left) for assumed Higgs boson masses of 115 GeV and 125 GeV. The background subtracted data are shown as points and the signal is shown as the red histograms. The blue lines indicate the uncertainty on the background prediction.

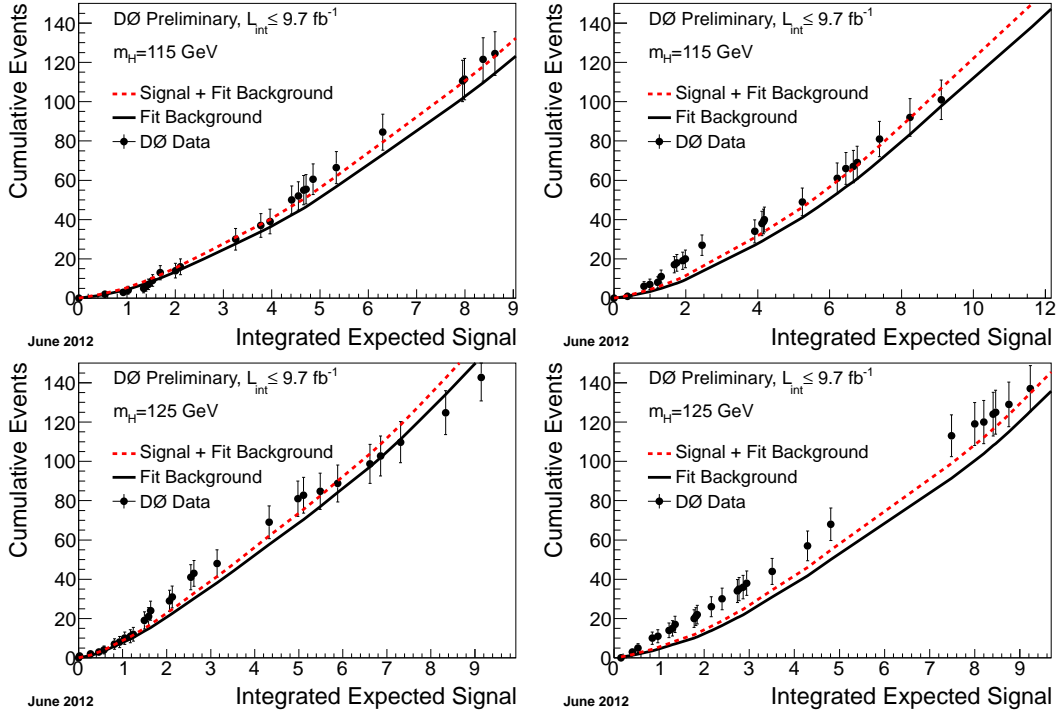


FIG. 18: Cumulative number of events for the highest  $s/b$  bins for this result (right) and the result from Ref. [8] (left) for assumed Higgs boson masses of 115 GeV and 125 GeV. The integrated background-only and signal+background predictions are shown as a function of the accumulated number of signal events. The points show the integrated number of observed events, including only the statistical uncertainty, which is correlated point-to-point. Systematic uncertainties on the integrated background-only and signal+background predictions are not displayed.

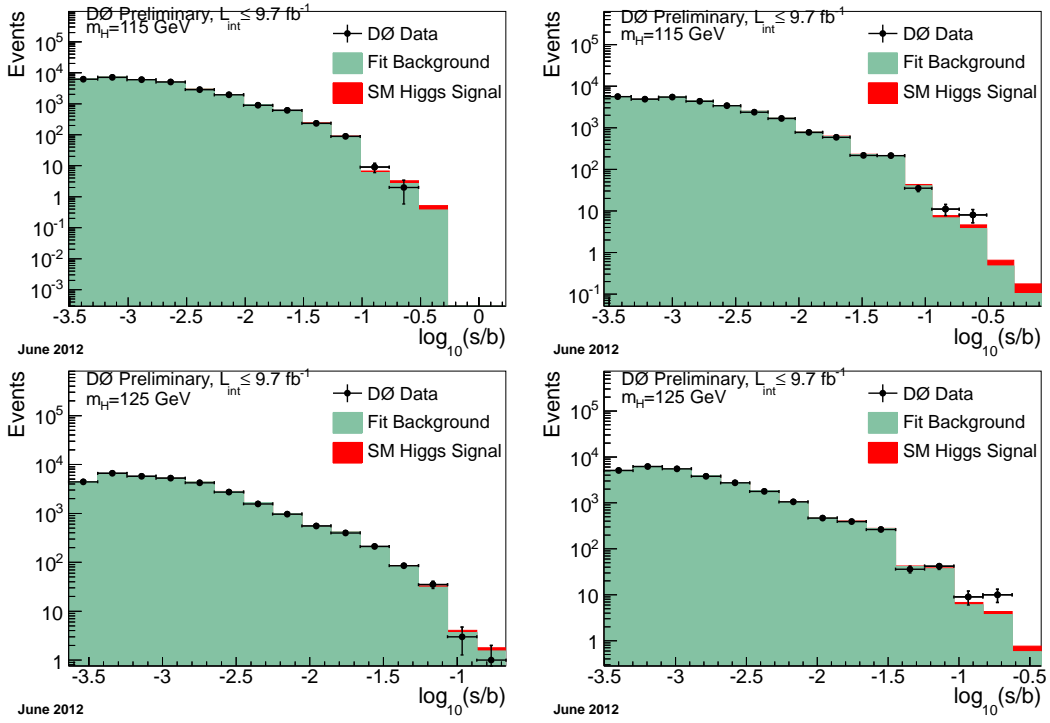


FIG. 19: Distributions of  $\log_{10}(s/b)$  in the combined  $WH/ZH, H \rightarrow b\bar{b}$  analyses for this result (right) and the result from Ref. [8] (left) for assumed Higgs boson masses of 115 GeV and 125 GeV. The data are shown with points and the expected signal is stacked on top of the sum of backgrounds. Only statistical uncertainties on the data points are shown.

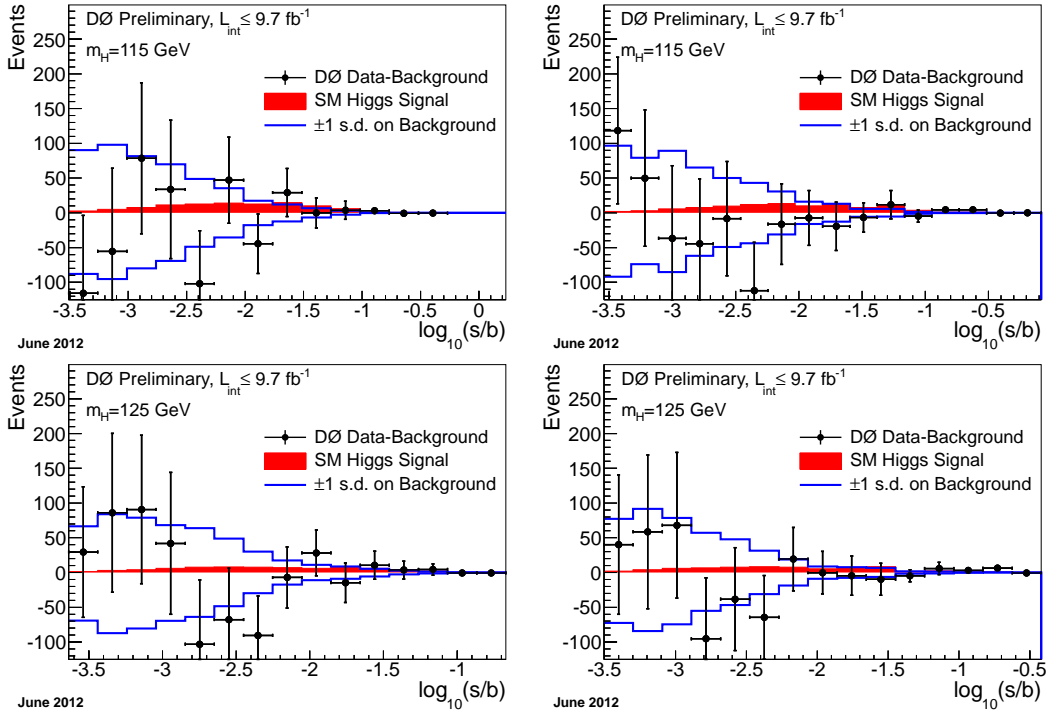


FIG. 20: Background-subtracted data distributions of  $\log_{10}(s/b)$  in the combined  $WH/ZH, H \rightarrow b\bar{b}$  analyses for this result (right) and the result from Ref. [8] (left) for assumed Higgs boson masses of 115 GeV and 125 GeV. The background subtracted data are shown as points and the signal is shown as the red histograms. The blue lines indicate the uncertainty on the background prediction.



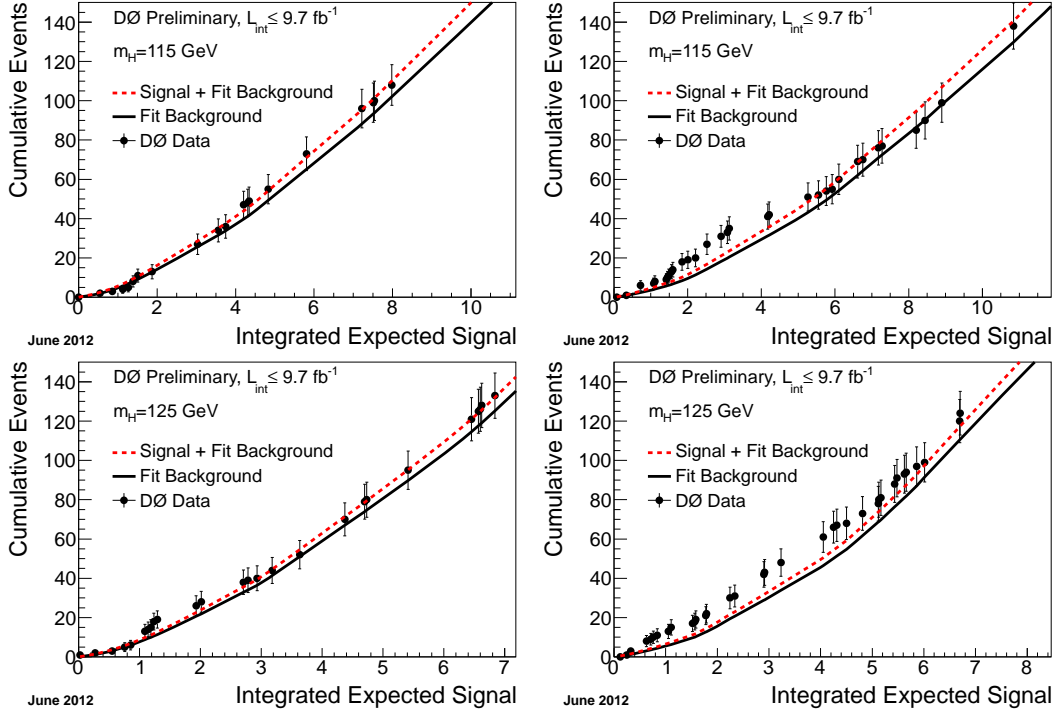


FIG. 21: Cumulative number of events for the highest  $s/b$  bins in the combined  $WH/ZH, H \rightarrow b\bar{b}$  analyses for this result (right) and the result from Ref. [8] (left) for assumed Higgs boson masses of 115 GeV and 125 GeV. . The integrated background-only and signal+background predictions are shown as a function of the accumulated number of signal events. The points show the integrated number of observed events, including only the statistical uncertainty, which is correlated point-to-point. Systematic uncertainties on the integrated background-only and signal+background predictions are not displayed.

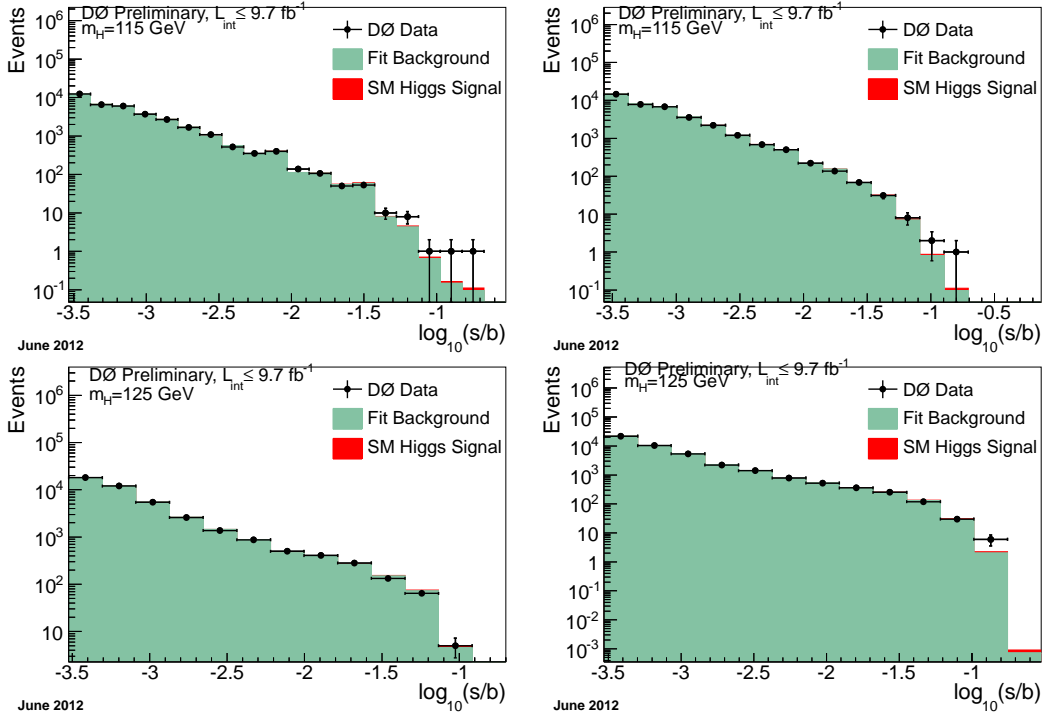


FIG. 22: Distributions of  $\log_{10}(s/b)$  in the combined  $WH/ZH/H, H \rightarrow W^+W^-$  analyses for this result (right) and the result from Ref. [8] (left) for assumed Higgs boson masses of 115 GeV and 125 GeV. . The data are shown with points and the expected signal is stacked on top of the sum of backgrounds. Only statistical uncertainties on the data points are shown.

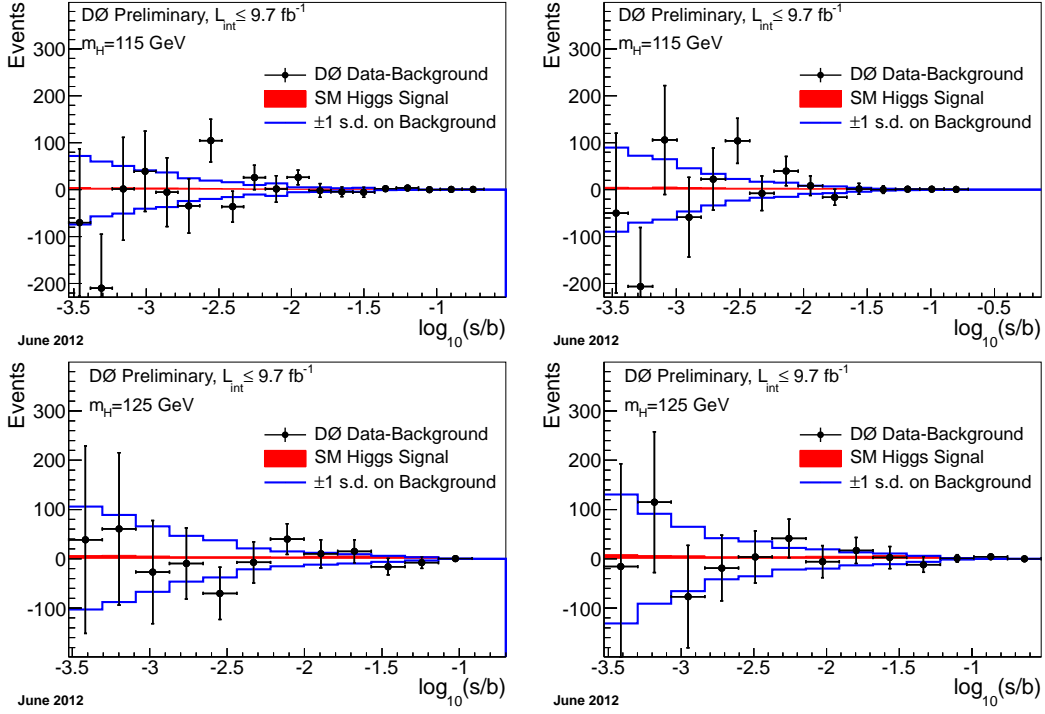


FIG. 23: Background-subtracted data distributions of  $\log_{10}(s/b)$  in the combined  $WH/ZH/H, H \rightarrow W^+W^-$  analyses for this result (right) and the result from Ref. [8] (left) for assumed Higgs boson masses of 115 GeV and 125 GeV. The background subtracted data are shown as points and the signal is shown as the red histograms. The blue lines indicate the uncertainty on the background prediction.

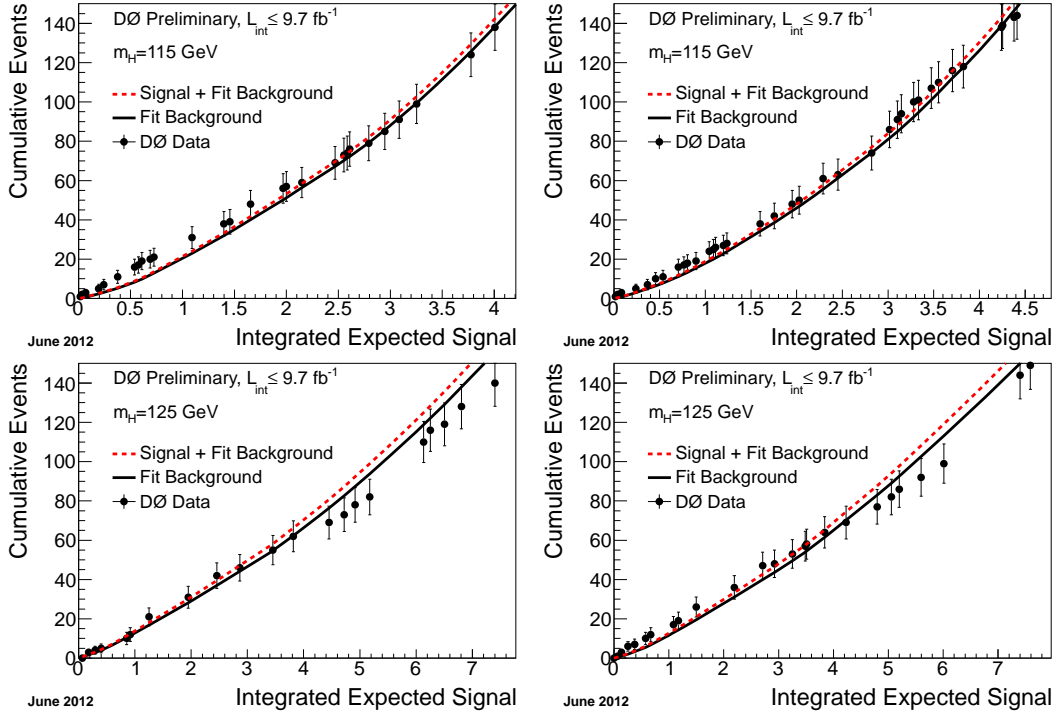


FIG. 24: Cumulative number of events for the highest  $s/b$  bins in the combined  $WH/ZH/H, H \rightarrow W^+W^-$  analyses for this result (right) and the result from Ref. [8] (left) for assumed Higgs boson masses of 115 GeV and 125 GeV. The integrated background-only and signal+background predictions are shown as a function of the accumulated number of signal events. The points show the integrated number of observed events, including only the statistical uncertainty, which is correlated point-to-point. Systematic uncertainties on the integrated background-only and signal+background predictions are not displayed.